Molecular Biology and Evolution, 2025, **42**, 1–18
https://doi.org/10.1093/molbev/msaf096
Advance access publication 25 April 2025
Discoveries

MBE OXFORD

Evolutionary and Functional Analysis of Caspase-8 and ASC Interactions to Drive Lytic Cell Death, PANoptosis

Sivakumar Prasanth Kumar [1], **Eswar Kumar Nadendla** [1], **R.K. Subbarao Malireddi** [1], **Syed Asfarul Haque** [2], **Raghvendra Mall** [1,4], **Andrew F. Neuwald** [3,*], **Thirumala-Devi Kanneganti** [1,*]

[1]Department of Immunology, St. Jude Children's Research Hospital, 262 Danny Thomas Place, Memphis, TN 38105, USA
[2]Cryo-Electron Microscopy Center, St. Jude Children's Research Hospital, 262 Danny Thomas Place, Memphis, TN 38105, USA
[3]Institute for Genome Sciences and Department of Biochemistry and Molecular Biology, University of Maryland School of Medicine, 670 W. Baltimore Street, Baltimore, MD 21201, USA
[4]Present address: Biotechnology Research Center, Technology Innovation Institute, Abu Dhabi, P.O. Box 9639, United Arab Emirates
***Corresponding authors:** E-mails: thirumala-devi.kanneganti@stjude.org; aneuwald@som.umaryland.edu.

Associate editor: Aida Ouangraoua

Abstract

Caspases are evolutionarily conserved proteins essential for driving cell death in development and host defense. Caspase-8, a key member of the caspase family, is implicated in nonlytic apoptosis, as well as lytic forms of cell death. Recently, caspase-8 has been identified as an integral component of PANoptosomes, multiprotein complexes formed in response to innate immune sensor activation. Several innate immune sensors can nucleate caspase-8–containing PANoptosome complexes to drive inflammatory lytic cell death, PANoptosis. However, how the evolutionarily conserved and diverse functions of caspase-8 drive PANoptosis remains unclear. To address this, we performed evolutionary, sequence, structural, and functional analyses to decode caspase-8's complex-forming abilities and its interaction with the PANoptosome adaptor ASC. Our study distinguished distinct subgroups within the death domain superfamily based on their evolutionary and functional relationships, identified homotypic traits among subfamily members, and captured key events in caspase evolution. We also identified critical residues defining the heterotypic interaction between caspase-8's death effector domain and ASC's pyrin domain, validated through cross-species analyses, dynamic simulations, and in vitro experiments. Overall, our study elucidated recent evolutionary adaptations of caspase-8 that allowed it to interact with ASC, improving our understanding of critical molecular associations in PANoptosome complex formation and the underlying PANoptotic responses in host defense and inflammation. These findings have implications for understanding mammalian immune responses and developing new therapeutic strategies for inflammatory diseases.

Keywords: caspases, ASC, PYCARD, DED filament, helical assembly, cell death, apoptosis, necroptosis, pyroptosis, PANoptosis, inflammasome, PANoptosome, evolution, arms race, coevolution, host-pathogen interactions, crosstalk, death fold, death domain superfamily, inflammation, inflammatory response, innate immunity, NLR

Introduction

Innate immunity forms the first line of defense against infection and disease (Kanneganti 2020). Cell death is a key component of the host innate immune response to clear intracellular pathogens and damaged cells. As a result, the ongoing coevolutionary arms race, where hosts adapt to infections and pathogens evolve strategies to evade immune defenses, leads to diversified host cell death signaling pathways (Daugherty and Malik 2012; Man and Kanneganti 2016; Place et al. 2021; Holland et al. 2024). Caspases (cysteine-dependent aspartyl-specific proteases; CASPs) are ancient regulators of programmed cell death, and some also drive inflammatory cytokine maturation. Many CASPs contain domains from the death domain (DD) superfamily, including CARD (caspase activation and recruitment domain) and DED (death effector domain). These domains, along with other family members such as DD and PYD (pyrin domain), are evolutionarily conserved across multicellular organisms, sharing a common 6 α-helical bundle topology and functioning as self-association and protein–protein interaction modules (Park et al. 2007; Hofmann 2020). Mammalian CASPs retain CARD and DED domains for scaffolding in cell death pathways (Kersse et al. 2011). $CASP1^{CARD}$-ASC^{CARD} interactions are central to inflammasome formation for lytic cell death (Martinon et al. 2002) and $CASP8^{DED}$-$FADD^{DED}$ (Fas-associated DD) interactions are known in apoptosis (Chinnaiyan et al. 1995; Boldin et al. 1996; Muzio et al. 1996; Kersse et al. 2011; Man and Kanneganti 2016). In simpler organisms such as *Caenorhabditis elegans*, which have 4 CASPs, CASPs handle all essential cell death functions (Horowitz and Shaham 2024). In mammals, with humans having 12 and mice having 10, CASPs have expanded and diversified through coevolution with pathogens, developing functional redundancies to enhance host defense (Eckhart et al. 2008; Man and Kanneganti 2016; Kesavardhana et al. 2020; Wang and Kanneganti 2021). However, the complexities of evolutionary conservation and divergence that have led to these functions remain unclear.

Received: December 9, 2024. **Revised:** April 9, 2025. **Accepted:** April 15, 2025

One of the key members of the CASP family is CASP8, which has roles in nonlytic apoptosis (Boldin et al. 1996; Muzio et al. 1996; Kesavardhana et al. 2020) and innate immune lytic cell death (Pierini et al. 2012; Man et al. 2013; Sagulenko et al. 2013; Gurung et al. 2014, 2016; Lukens et al. 2014; Kuriakose et al. 2016; Newton et al. 2019), including PANoptosis. PANoptosis is a lytic, innate immune cell death pathway initiated by innate immune sensors and driven by CASPs and RIPKs through PANoptosomes (Kuriakose et al. 2016; Christgen et al. 2020; Karki, Sharma et al. 2021; Karki, Sundaram et al. 2021; Lee et al. 2021; Karki et al. 2022; Sharma et al. 2025). PANoptosis provides host defense against infections but can also drive inflammation and inflammatory disease, making it a potential therapeutic target (Christgen et al. 2020; Malireddi et al. 2020; Zheng et al. 2020; Karki, Sharma et al. 2021; Karki, Sundaram et al. 2021; Lee et al. 2021; Karki et al. 2022; Chen et al. 2023; Sundaram et al. 2023, 2024; Sharma et al. 2025). CASP8 is an integral component of the PANoptosome complexes that drive PANoptosis, and the adaptor ASC, a PYD and CARD-containing protein, is also found in many PANoptosomes (Christgen et al. 2020; Malireddi et al. 2020; Zheng et al. 2020; Lee et al. 2021; Sundaram et al. 2023, 2024; Sharma et al. 2025). Biochemical and structural studies have found that the DEDs of CASP8 and the PYD of ASC interact (Vajjhala et al. 2015; Fu et al. 2016) to facilitate assembly of cell death complexes. This heterotypic interaction challenges the concept of exclusivity in the DD superfamily (Kersse et al. 2011), where homotypic interactions typically guide complex formation (e.g. ASC^{CARD}-$CASP1^{CARD}$, $CASP8^{DED}$-$FADD^{DED}$, $NLRP^{PYD}$-ASC^{PYD}) (Park et al. 2007). However, how CASP8 performs evolutionarily conserved and diverse functions to drive PANoptosis in health and disease remains unclear.

In this study, we performed Bayesian inference-based evolutionary analysis of the DD superfamily to identify functional subgroups, such as DED and PYD domains, based on their evolutionary and functional relationships. We also sought to capture homotypic traits among subfamily members and highlight key events in caspase evolution. We further defined the homotypic interaction within CASP8 and heterotypic interaction between $CASP8^{DED}$ and ASC^{PYD} through Bayesian evolutionary analysis, residue couplings, and sequence and structural analysis. We also used functional experiments, including size exclusion chromatography, negative staining electron microscopy, and pull down assays, to validate the evolutionary, sequence, structural, and functional relationships. Statistical inference methods provided functional clues about the evolutionarily conserved residue patterns at the interaction interface, and we validated these through cross-species analyses, dynamic simulations, and in vitro studies. Mutating specific residues functionally disrupted CASP8 stability and oligomerization, which may play a critical role in preventing its downstream functions. These results provide insights into the significance of CASP8 and potential CASP8-ASC interaction residues in modulating PANoptosome activity and related immune responses in health and disease.

Results and Discussion

Hierarchical Classification of the DD Superfamily Using the BPPS Method

CASP8 has likely undergone evolutionary pressures in early vertebrates, with negative selection maintaining its essential role as a specialized initiator and its inflammatory functions (Aravind et al. 2001; Sakamaki and Satou 2009; Sakamaki et al. 2015; Kesavardhana et al. 2020). This specialization may result from conserving and diverging amino acid residues at key positions (Neuwald 2014a,b; Neuwald et al. 2022) that influence CASP8's molecular functions. To identify these key residues, we used BPPS (Bayesian Partitioning with Pattern Selection), a statistical inference method that identifies conserved residue patterns among evolutionarily related proteins from functional divergence events (Neuwald et al. 2018). BPPS operates on the assumption that a protein superfamily diverges into subgroups, each potentially adapting its structural fold for specific roles. These subgroups may undergo further divergence, conserving crucial residues at critical sites for original and new functions. Multiple rounds of such divergence events could lead to a tree-like structure of hierarchically arranged subgroups (hereafter referred to as a hierarchical tree), each featuring distinct residues at specific positions (Neuwald et al. 2018). BPPS analyzes multiple sequence alignments (MSA) from protein superfamilies, partitioning them into hierarchically nested MSAs (hiMSA) based on correlated residue patterns that may be unique to each subgroup (Neuwald 2014a,b; Neuwald and Altschul 2016; Neuwald et al. 2020). A scheme of the overarching approaches used throughout the study to identify residue patterns and other functionally relevant residues is shown in Fig. 1.

We first sought to identify subgroups of DD superfamily members from the MSA by creating a hierarchical tree using the BPPS method (Neuwald et al. 2018), which models organism classification levels (superfamily, family, and subfamily) based on evolutionary relationships. The DD sequences obtained from protein databases and sequence similarity searches were aligned and supplemented with known and predicted death fold structures. These were used as the input for BPPS calculations to generate a hierarchical tree with different subgroups, capturing evolutionary features. The topmost node in the hierarchical tree likely signifies the superfamily, while descending nodes may represent lower levels, such as family and subfamily. Here, a subfamily refers to a group of sequences within a family that share more recent common evolutionary ancestors and feature specific residue patterns distinguishing them from other related subfamilies. The resulting DD tree consisted of a single superfamily, 26 family, and 95 subfamily groups (supplementary fig. S1, Supplementary Material online). The expansion of death fold proteins in chordate- and vertebrate-specific lineages appears to have contributed to an increased number of immune-related proteins, adding complexity to the immune system and its cell death pathways (Aravind et al. 2001). This trend can be observed in the prepared superfamily MSA, which shows the highest proportion of diverse chordate sequences (supplementary fig. S2a, Supplementary Material online). Given this complexity, we aimed to study how the domains of CASP8 and ASC, critical molecules in the formation of cell death complexes, are likely evolutionarily related by examining their subgroups in the hierarchical tree, which may contribute to key molecular associations underpinning inflammasome and PANoptosome formation. We therefore focused on examining subfamily groups containing mouse CASP8 death effector domains (DED1, node 21; DED2, node 67) and ASC pyrin domain (PYD, node 37) sequences. These were grouped within DEDs (DED1, node 2; DED2, node 38) and PYD (node 3) family subgroups, respectively. Within the DED and PYD family subgroups, other closely related proteins were grouped. For instance, the DED1 family subgroup (node 2) included FADD, PEA-15 (phosphoprotein enriched in

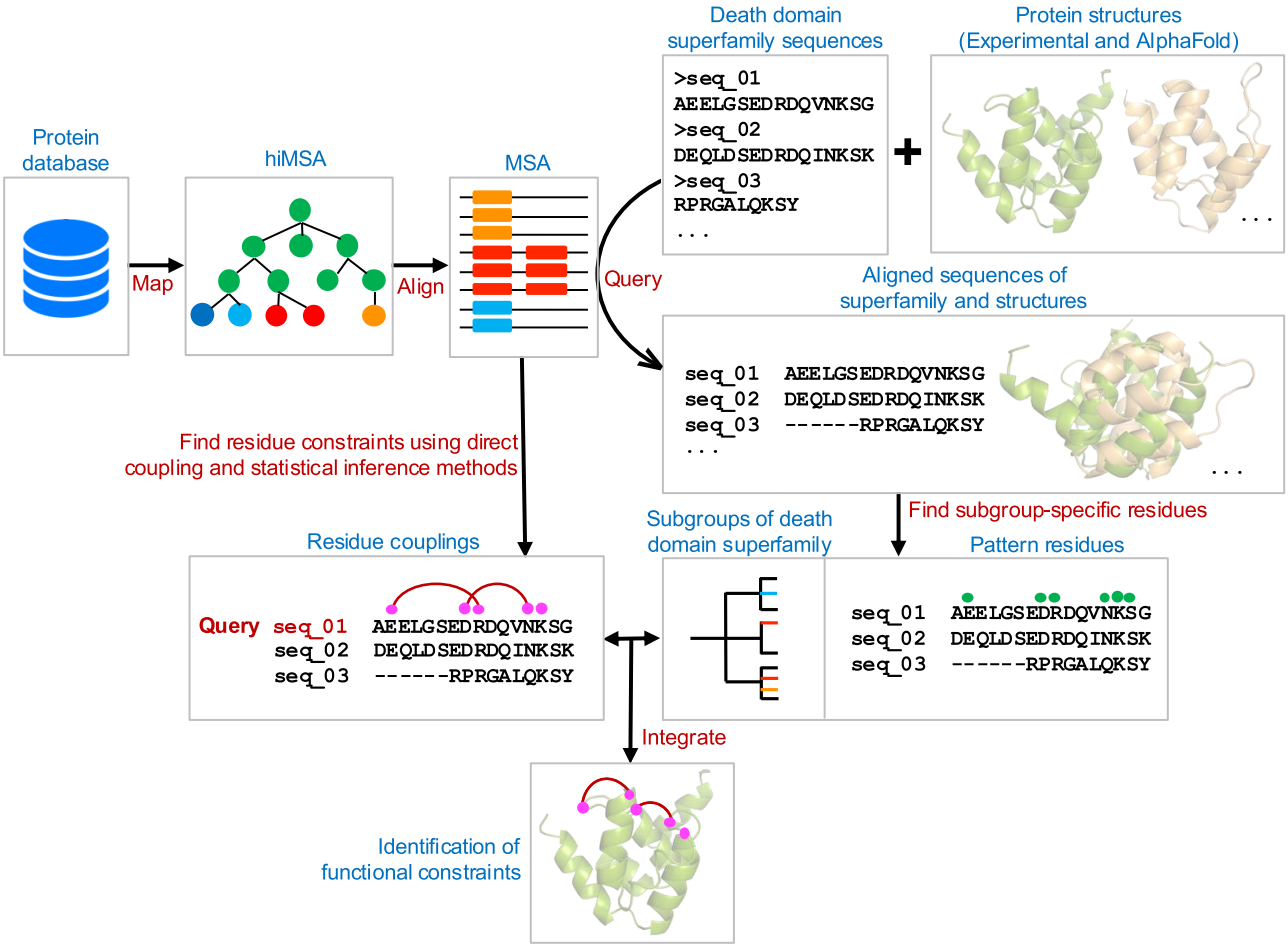

Fig. 1. Workflow integrating statistical inference methods. Initially, protein sequences from the NCBI protein database were mapped to DDs using the CDD2MGS program, generating a hiMSA. Next, sequences from the DD superfamily (IPR011029) were retrieved from the InterPro database and augmented with protein structures (experimentally determined and protein models obtained from AlphaFold). These sequences were then aligned against hiMSA, resulting in an MSA. A hierarchical tree was built from the MSA using the BPPS program to identify subgroups representing different family members of the DD superfamily and to identify statistically significant pattern residues within each subgroup. The query-based DARC program was applied to identify pattern residues and residue couplings from mCASP8^{DED} and mASC^{PYD} sequences. Finally, the correspondence between different methods and identified pattern residues was utilized to prioritize the best-scoring amino acid residues for in vitro experiments.

astrocytes, 15 kDa), among others, in addition to mCASP8^{DED1}. BPPS selects a set of pattern residues to define subgroups, guided by the log-probability ratio (LPR). The LPR evaluates the likelihood of observing the pattern residues under the subgroup model versus a model representing other closely related, divergent subgroups (Neuwald 2014a). Because the LPR is computed using the natural logarithm, it is measured in nats, which has an information theoretic interpretation. The supplementary fig. S2b, Supplementary Material online shows selected representative subgroups of the hierarchical tree with its LPR scores. The exclusive enrichment of chordate sequences in CASP8^{DEDs} and ASC^{PYD} subgroups may suggest their ability to capture evolutionary pattern residues specific to chordates (Reed et al. 2004; Park et al. 2007). This enrichment was also reflected in the percentage distribution of sequences within the major phylum of the death fold superfamily (supplementary fig. S3, Supplementary Material online).

Identification of DD Subgroups and Functional Enrichment

The hierarchical tree's subgroups hint at the possibility of an ancestral form of the trait among DD proteins within the same node. As previously mentioned, our analysis focused on subfamily groups within the DED1 (node 2), PYD-ASC (node 3), and DED2 (node 38) families, distinguishing distinct functional subgroups at each family node (supplementary fig. S1, Supplementary Material online). Within the DED1 family, the subfamily group (node 21) includes CASP8^{DED1} sequences from human and mouse, as well as those from other mammals, birds, amphibians, and reptiles. Based on their placement within the same family node in the hierarchical tree (supplementary fig. S1, Supplementary Material online), we observed the DED domains of CASP8, FADD, and PEA-15 exhibit a coevolutionary relationship; given that all 3 of these proteins have been implicated in forming the death-inducing signaling complexes (DISC), these findings might suggest coevolution in forming DISC. This could be distinct from other immune signaling DED domain proteins and aligns with the expansion of apoptotic regulators in multicellular organisms, responding to various stimuli through the death receptor-mediated extrinsic apoptotic pathway (Kesavardhana et al. 2020; Tummers et al. 2020). The tree (supplementary fig. S1, Supplementary Material online) also identified the DED in the lancelet ubiquitinyl hydrolase 1 as a distinct subfamily group (node 55), suggesting likely horizontal gene transfer

and adaptive changes in innate immune genes in amphioxus (Xiong et al. 2023). Homotypic traits among subfamily members of the DD superfamily were captured at the family level of the tree, which could align with their evolutionary and functional relationships. For instance, CASP8^{DED1} and its homotypic interaction partner FADD^{DED} are grouped under the same DED1 family (node 2), while NLRP3^{PYD} and its partner ASC^{PYD} are grouped together in the PYD family (node 3).

Within the DED2 family, the subfamily group (node 67) contained human and mouse CASP8^{DED2} sequences, along with those from other mammals, reptiles, and a few nonperching birds (e.g. rail) (supplementary fig. S1, Supplementary Material online). This suggests the possibility that conserved residues required for CASP8^{DED2} function may be shared among these groups. Furthermore, the tree identified a subfamily group (node 53) consisting entirely of perching birds (e.g. crow) and a subfamily group (node 98) containing CASP8-like^{DED2} and CASP10^{DED2} sequences exclusively from ray-finned fishes (e.g. toothcarps, salmonids, labyrinth fish, among others; supplementary fig. S1, Supplementary Material online).

The hierarchical tree structure may also have captured key events in CASP evolution. For example, the split between the subgroup exclusive to fish (node 98) and the one shared with mammals and birds (node 67) may suggest that fishes underwent adaptations in DED2 sequences. These adaptations could be linked to earlier evolutionary events, such as genome duplication and gene arrangements within the fish lineage (Spead et al. 2018), although further studies are needed to confirm this connection.

In addition to using this hierarchical tree, we also applied a traditional phylogenetic approach to study the evolutionary and functional relationships among N-terminal CARD and DED domains of CASPs. The phylogenetic tree captured relationships among CASPs (supplementary fig. S4, Supplementary Material online), similar to those seen in the hierarchical tree (supplementary fig. S1, node 38 Supplementary Material online). In both trees, the DED-containing CASPs (CASP8 and CASP10) clustered similarly, reflecting their known functional roles in cell death regulation (Kischkel et al. 2001; Fischer et al. 2006; Man and Kanneganti 2016; Kanneganti 2020; Kesavardhana et al. 2020). These findings collectively suggest that death fold domains in CASPs have evolved to maintain and specialized cell death functions.

In the hierarchical tree, we also observed that, within the PYD family, PYD domains of ASC and NLRPs were mapped into distinct subfamily groups (supplementary fig. S1, node 3 Supplementary Material online). Although both of these molecules oligomerize through their PYD domains to form signaling platforms for inflammasomes (Martinon et al. 2001, 2002; Dick et al. 2016) and PANoptosomes (Christgen et al. 2020), we found that their evolutionary signatures differed, since they were grouped into distinct subfamilies (supplementary fig. S1, Supplementary Material online). These differences likely reflect their distinct molecular roles. The N-terminal PYD in NLRPs regulates conformational states for molecular processes such as innate immune sensing and inflammasome formation (Martinon et al. 2001, 2002; Andreeva et al. 2021). In contrast, the PYD of ASC interacts with NLRP PYDs to act as a scaffold to recruit CASP1 and mediate downstream cell death functions (Martinon et al. 2001, 2002; Dick et al. 2016). Certain NLRPs, including NLRP3, NLRP6, and NLRP12, were assigned to the same subgroup (node 105) in the hierarchical tree (supplementary fig. S1, Supplementary Material online), suggesting shared coevolutionary functions that remain to be fully determined. Furthermore, certain subgroup members, including NLRP3 and NLRP12, have recently been proposed to act as part of an NLR network in response to heme-containing triggers to form a PANoptosome with NLRC5 and drive PANoptosis (Sundaram et al. 2023, 2024). These insights from the hierarchical tree and subgroup identification offer a potential enhancement in understanding the molecular mechanisms underlying immune responses and may reflect the evolutionary significance of death family members.

CASP8^{DED} and ASC^{PYD} Contain Unique Residue Patterns

Following taxonomic analysis of DED and PYD subfamilies, we identified pattern residues unique to each domain in CASP8 and ASC (supplementary table S1, Supplementary Material online). The information (in nats) contributed to a subgroup's LPR by an individual pattern position reflects the subgroup-specific selective pressure imposed at that position (Neuwald 2014a; Neuwald and Altschul 2016). Nats for a pattern residue are calculated as the natural logarithm of the likelihood ratio between the foreground and background models, with higher values indicating that the residue is more likely under the subgroup model than under the background model. As an example, a score of 55.5 nats for phenylalanine at position 120 of mCASP8^{DED2} indicates that the residue composition observed at that position in the subgroup's alignment is $e^{55.5} \approx 10^{24}$ times more likely to be generated by the subgroup model (termed the foreground) than by a model based on other, closely related subgroups (termed the background). We analyzed the top 10 pattern residues ranked by information measure (supplementary table S1, Supplementary Material online) and mapped them onto the mCASP8^{DED}-mASC^{PYD} complex model as well as select DED1 and DED2 family members (supplementary fig. S5, Supplementary Material online) using the PyMOL program (Schrödinger 2024a). Our goal was to find residues unique to subgroups within the domains of the mCASP8^{DED}-mASC^{PYD} complex. These residues are thought to coevolve, potentially creating an evolutionary signature for CASP8-ASC that may facilitate intermolecular interactions contributing to PANoptosome assembly and initiating an immune response. The pattern residues of mCASP8^{DED2} (E116, N168, and S170) were identified at the mCASP8^{DED}-mASC^{PYD} complex interface, while neither mASC^{PYD} nor mCASP8^{DED1} had residues at the interface (supplementary fig. S5a, Supplementary Material online). Instead, their residues were predominantly mapped to the core and surfaces of DED and PYD filaments (supplementary fig. S5a, Supplementary Material online), which suggests a possible preference for oligomerization over complex interaction. This underscores the evolutionary emphasis on conserving residues for DED and PYD filament oligomerization, a preference also observed across different DED1 and DED2 family members in various species (supplementary fig. S5b, Supplementary Material online). Although pattern residues conserved over long evolutionary periods are presumably shaped by functional constraints, those conserved across closely related organisms may reflect recent common descent. In such cases,

inferring a functional role requires further support from biochemical and structural studies.

In addition to identifying conserved pattern residues via BPPS, we also performed site-specific positive selection analysis of $CASP8^{DED2}$ orthologs using the FUBAR program (Murrell et al. 2013). While BPPS identified pattern residues that are conserved within the $CASP8^{DED2}$ subgroup and may reflect functional specialization, FUBAR detects sites under positive and negative selection pressure, providing evolutionary insights that complement the BPPS findings. This allowed us to investigate whether any $CASP8^{DED2}$ interface residues in the CASP8-ASC complex were also evolving under diversifying selection. We identified 4 sites as positively selected (diversifying) sites (supplementary fig. S6a and b, Supplementary Material online) and 42 negatively selected (purifying) sites at a posterior probability threshold of 0.9. Though these 4 positively selected sites are highly diverse across species (supplementary fig. S6c, Supplementary Material online), 2 sites (D165 at the $mCASP8^{DED2}$-$mASC^{PYD}$ interface and N126 at the $mCASP8^{DED2\text{-}DED1}$ interface) mapped to heterotypic interfaces (supplementary fig. S6b, Supplementary Material online), suggesting functional relevance. However, since BPPS pattern residues were more directly associated with subgroup-specific conservation across species, we prioritized these residues for further analyses.

Mapping and Analysis of Pattern Residues in $mCASP8^{DEDs}$ and $mASC^{PYD}$ Domains

Superfamily analysis using the BPPS method (Neuwald et al. 2018) identified residue patterns that distinguish subfamilies within the DD superfamily. However, these pattern residues were not observed at the domain interface when mapped to the $mCASP8^{DED}$-$mASC^{PYD}$ model complex, with the exception of residues in $CASP8^{DED2}$ (supplementary fig. S5a, Supplementary Material online). To gain evolutionary insights into their domain interface and study potential relationships between protein structure, function, and evolution, we used the DARC (Deep Analysis of Residue Constraints) method, integrating sequence-based residue coupling, Bayesian inference, and structure-based sequence constraints (Tondnevis et al. 2020). The coupling technique identifies evolutionarily constrained residue pairs that are likely to interact; this suggests that they might impact domain structure and function (Neuwald and Altschul 2018). Further, DARC employs a Bayesian sampler in a query-centric approach, creating subgroups that include the query sequences ($mCASP8^{DED}$ and $mASC^{PYD}$) at 2 levels of hierarchy: superfamily and family. Based on the DARC findings, we further investigated the family subgroup of each domain within the $mCASP8^{DED}$-$mASC^{PYD}$ complex to examine the roles these pattern residues may play in domain interactions (Fig. 2). The death fold and ASC^{PYD} MSAs, along with the complex models (discussed in Section "Models of $mCASP8^{DED}$-$mASC^{PYD}$ complex" below), were used as input for the DARC calculations. Similar to the steps used in the superfamily analysis, the top 5 pattern residues ranked by the information measure were identified in the contrast alignment (Fig. 2), which was observed consistently in 1,000 independent runs with random seeds. This alignment, which incorporates both foreground (conserved residues) and background (divergent residues) information, illustrates the degree of selective pressure acting on foreground residue positions (Fig. 2).

Models of the $mCASP8^{DED}$-$mASC^{PYD}$ Complex

We built 3 complex structure models (Fig. 3; supplementary fig. S7, Supplementary Material online) using protein–protein docking, protein superimposition, and AlphaFold (Evans et al. 2022) modeling techniques, and used them as inputs to DARC calculations. This elucidated the potential spatial role of top-scoring pattern residues unique to each domain of the $mCASP8^{DED}$-$mASC^{PYD}$ complex in mediating interdomain interactions. After building homology models of $mCASP8^{DED}$ using the cryo-EM structure of the $hCASP8^{DED}$ filament (PDB: 5l08) (Fu et al. 2016), we developed the $mCASP8^{DED}$-$mASC^{PYD}$ complex model (supplementary fig. S7a, Supplementary Material online) through a protein–protein docking procedure with residue constraints (specifically, R41 of ASC^{PYD} and F143 of $CASP8^{DED}$), based on previous biochemical reports (Vajjhala et al. 2015). Mutating residue R41 in ASC effectively reduces procaspase-8 binding (Vajjhala et al. 2015). However, the exact CASP8 residue(s) involved in this binding process have not been determined experimentally. The second complex model was then generated by aligning the $mASC^{PYD}$ domain onto the top layer of the $mCASP8^{DED}$ filament (Fig. 3), while the third model was built using the AlphaFold2 multimer module (Evans et al. 2022) (supplementary fig. S7b, Supplementary Material online). Consistent with earlier biochemical data (Sagulenko et al. 2013; Vajjhala et al. 2015; Fu et al. 2016), all these complex models position one ASC^{PYD} domain at the DED domain interface of CASP8, suggesting a possible interaction scenario. Once the complex models were built, we adopted the schematic of the helical assembly proposed for death fold proteins (Ferrao and Wu 2012; Hollingsworth et al. 2021) to distinguish different interface types (e.g. I, II, and III). Given that DDs exhibit 3 asymmetric interfaces across 6 α-helices arranged in an antiparallel fashion, the interface types are further characterized by their sides, designated as "a" and "b" (Fig. 3). Within a filament, type I interfaces mediate lateral interactions between domains, while type II and III interfaces are vertical, facilitating interstrand interactions between 2 chains (Park et al. 2007; Kersse et al. 2011; Ferrao and Wu 2012). Our models suggest that ASC^{PYD} interacts with $CASP8^{DED}$ using type II and III interfaces (Fig. 3a and b). The upper and lower ends of the $mCASP8^{DED}$ filament expose type II and III interfaces, which are available to interact with $mASC^{PYD}$ to assemble an elongated, heterogeneous filament along the helical axis. The $mCASP8^{DED}$-$mASC^{PYD}$ complex models provide alternative placements of $mASC^{PYD}$ within the $mCASP8^{DED}$ filament, with the docking model positioning $mASC^{PYD}$ at the lower end (supplementary fig. S7a, Supplementary Material online), and the superimposed (Fig. 3) and AlphaFold2 model (supplementary fig. S7b, Supplementary Material online) placing it at the upper end. Notably, the AlphaFold2 model closely resembles the superimposed model but exhibits a 90° rotational shift in the orientation of the $mASC^{PYD}$ domain (supplementary fig. S7b, Supplementary Material online).

Residue Couplings and Functional Determinants of $mCASP8^{DED}$-$mASC^{PYD}$ Complex Formation

Following the interface identification in modeled complexes, we analyzed the pattern residues in relation to proposed domain interfaces and their involvement in residue couplings. To identify the most suitable model for promoting $mCASP8^{DED}$ filament nucleation by the $mASC^{PYD}$ filament and subsequent filament elongation, each complex model was

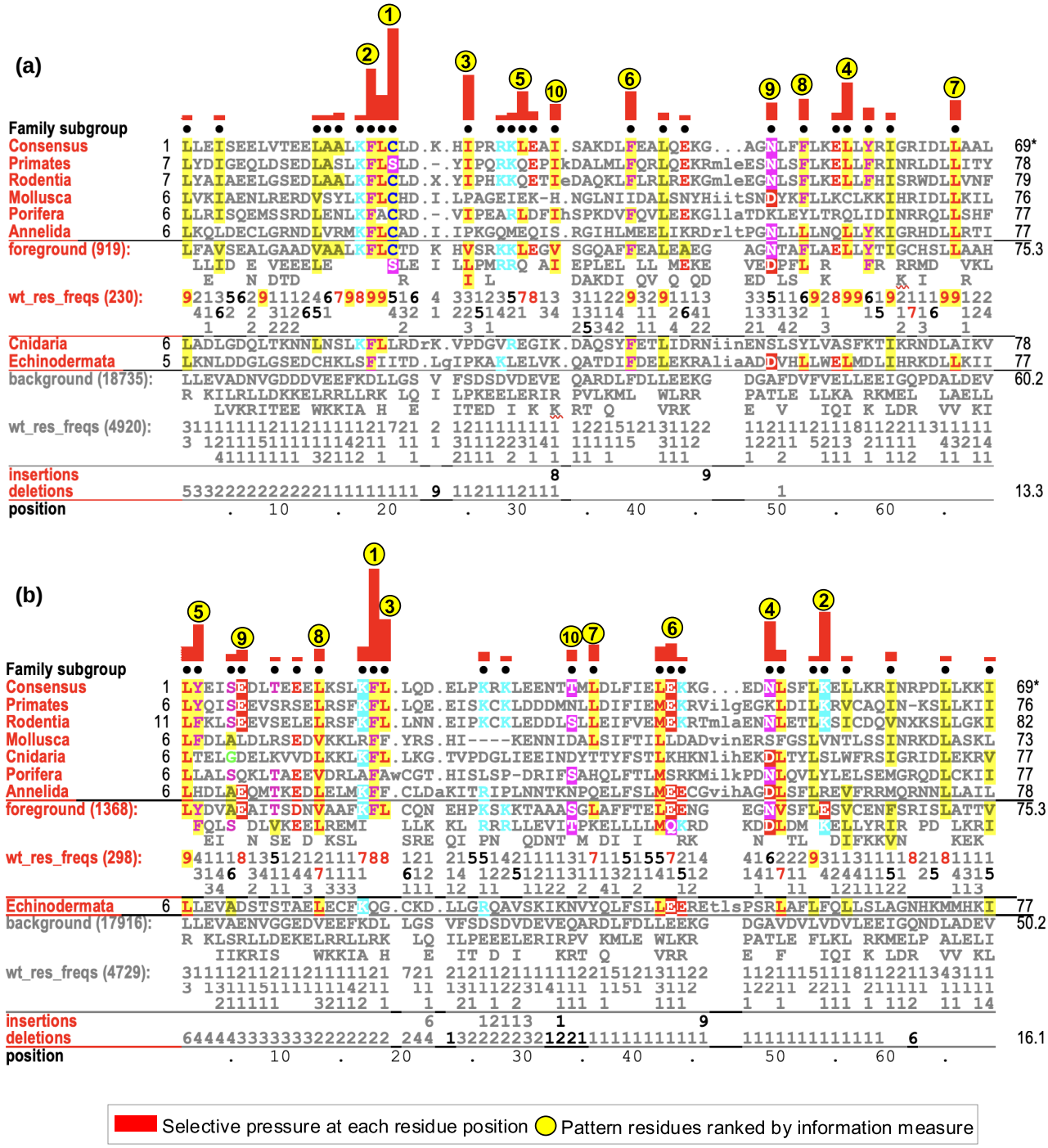

Fig. 2. Alignment of CASP8^{DED} family sequences among representative taxa of the DD superfamily. a and b) Contrast alignment of (a) mCASP8^{DED1} and (b) mCASP8^{DED2} family sequences obtained using query-based analysis. The consensus family sequence of the CASP8^{DED} is labeled as "Consensus" with residue positions corresponding to columns of the MSA. Protein sequences from these phyla (Primates, *Homo sapiens*; Rodentia, *Mus musculus*; Mollusca, *Octopus vulgaris*; Porifera, *Amphimedon queenslandica*; Cnidaria, *Hydra vulgaris*; Annelida, *Capitella teleta*; Echinodermata, *Acanthaster planci*) were chosen as the displayed foreground sequences. The CASP8 homolog in *Drosophila melanogaster* (Arthropoda phylum), DREDD/DCP2 did not align well with this contrast alignment. Rotifers, Nematodes, and Platyhelminthes do not contain DED-containing CASP8 proteins and thus, are not included in this alignment. Red vertical bars represent the selective pressure on the pattern residue, calculated using a semi-logarithmic scale (higher bars reflect stronger selective pressure). This selective pressure reflects the degree to which residue frequencies at each position in the foreground diverge from those at the corresponding positions in the background. The pattern residues are ranked by information measure, as highlighted in the yellow circles (highest information measure is ranked #1). Amino acid residues in the alignment are colored based on the scheme of biochemical similarities. Below the alignment, 2 blocks of alignment (foreground and background) are given starting with sequences indicating characteristic residues at each position of the alignment. Under to the sequence field within each alignment block, the numbers designate the frequencies (after weight-based correction for sequence redundancy) of residues expressed in integer tenths (a value of 2 indicates the corresponding residue is found in 20% to 30% of the aligned sequences). Under the background alignment block, the "insertions" and "deletions" rows indicate the frequencies of corresponding insertions and deletions, respectively, at each aligned residue position, expressed in integer tenths. Frequencies below 10% are omitted for clarity.

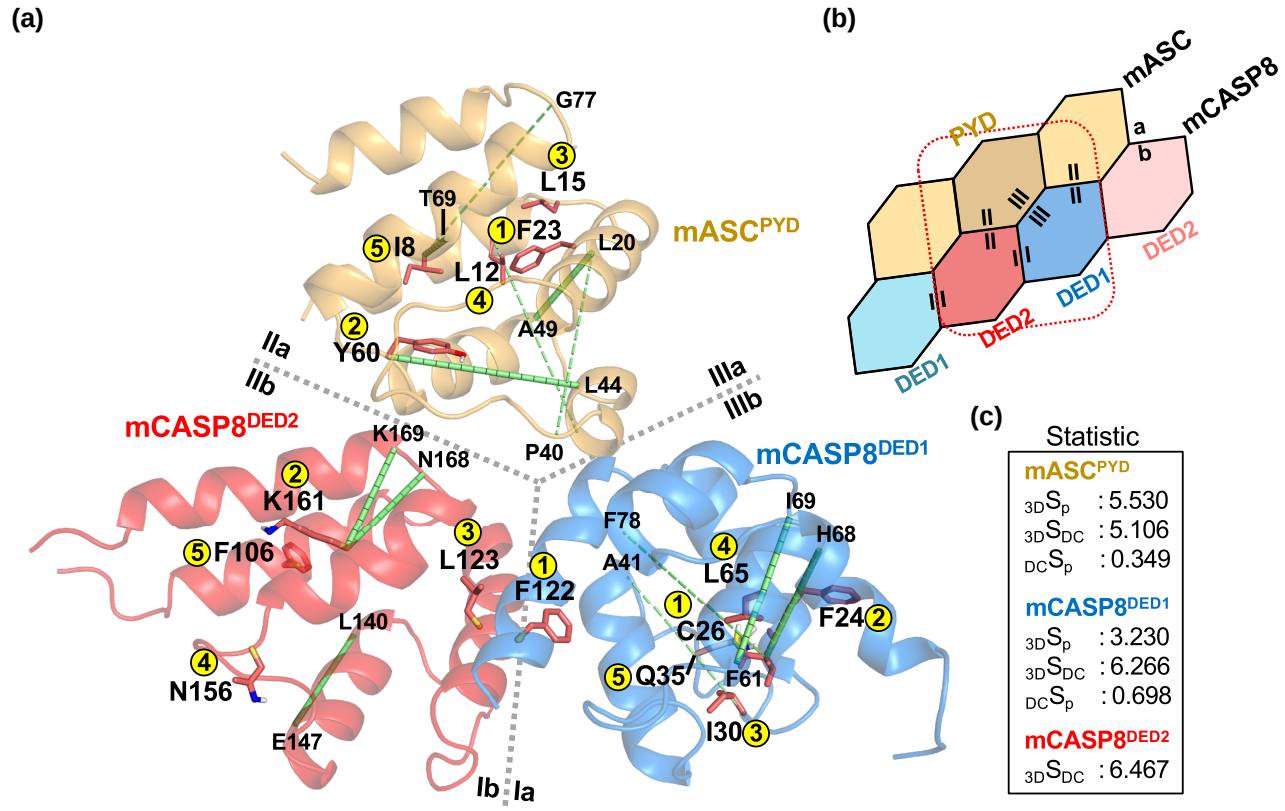

Fig. 3. Pattern and directly coupled (DC) residues identified from query-based analysis mapped onto the mCASP8^{DED}-mASC^{PYD} complex (superimposed model). a) Protein domains and pattern residues are shown in cartoon and stick representations, respectively. The pattern residues are ranked by information measure, as highlighted in the yellow circles (highest information measure is ranked #1). Residues of DC pairs with a distance below 10 Å and equal to or above 10 Å are shown in thick and dashed green rods, respectively. b) Schematic of the heterotypic interfaces of the mCASP8^{DED}-mASC^{PYD} complex. c) Various statistical measures (S) computed for correspondences between pattern (p), directly coupled (DC), and 3D clustered residues.

thoroughly examined. This process led to the identification of several key interface residues, as discussed in subsequent sections. Due to variations in mASC^{PYD} placement among complex models, discussions related to interfaces are tailored to each specific model.

Across all complex models, the most-constrained residue, F23, was in the hydrophobic core of mASC^{PYD}, displaying a high degree of conservation across diverse taxa (supplementary fig. S8, Supplementary Material online). Further, pattern residues such as I8, L12, and L15 (ranked fifth, third, and second) occupied interface type IIIb in the mASC^{PYD} filament form (PDB: 2n1f; supplementary fig. S7a, Supplementary Material online; Sborgi et al. 2015). Positioned next to the type IIIb pattern residues, the E13 residue exhibits pronounced effects on ASC self-association upon mutation (Vajjhala et al. 2015). However, the mechanistic role of E13 in heterodomain interactions with mCASP8^{DEDs} remains unclear. Notably, this interface extensively interacts with its counterpart, interface type IIIa, in its filament form, where residue R41 modulates procaspase-8 binding when mutated (Vajjhala et al. 2015). Furthermore, residue couplings were identified across distinct interfaces in the ASC^{PYD} filament, which were consistently observed in 1,000 independent calculations, including within type I, between types I and II, types I and III, types II and III, and within type III interfaces. Overall, these results suggest that the DARC method prioritized evolutionarily related residues in interfaces that are likely important for mASC^{PYD} domain stability, oligomerization, and filament assembly (Fig. 3; supplementary fig. S7, Supplementary Material online).

The most-constrained residue in mCASP8^{DED1} is C26 (S26 in humans) (Fig. 2a). The pattern residues, I30 (interface III) and F24 (I), are located at the interface of mASC^{PYD} and mCASP8^{DED2} (supplementary fig. S7a, Supplementary Material online). F122 is the most-constrained (Fig. 2b) and type Ib residue of mCASP8^{DED2}, packed against Y8 of type Ia from the adjacent mCASP8^{DED1} (Fig. 3; Y8 is not a pattern residue and is therefore not directly shown in the figure). Both F122 (alone) and Y8 (when combined with other positions) can impair hCASP8^{DED} filament formation upon mutation (Fu et al. 2016). The identification of sites that have been experimentally confirmed to be critical for filament formation as pattern residues supports the validity of the adopted statistical approaches. E147 is the only pattern residue from the type II interface facing mASC^{PYD}. The pattern residues and their couplings from this model are similar in superimposed (Fig. 3) and AlphaFold2 (supplementary fig. S7b, Supplementary Material online) models. The second ranked pattern residue, K161, is located at the mCASP8^{DED2}-mASC^{PYD} domain interface of the superimposed model (Fig. 3). In summary, the DARC method pinpointed key residues potentially involved in filament disruption and identified deterministic residue patterns under selective pressure.

Residue Pattern for mCASP8^{DED} Stability

Leveraging both superfamily and query-based methods, we elucidated valuable insights into the evolutionary and structural aspects of select pattern residues, distinguishing them

into 2 separate components: the stability and oligomerization of mCASP8^{DED} filaments and mCASP8^{DED}-mASC^{PYD} domain interactions. In the first component, we successfully identified the key residue F122, which governs the stability of mCASP8^{DED} filaments (Fu et al. 2016), as the most-constrained residue (Figs. 2b and 3) from the DARC method. We further conducted a cross-species analysis of CASP8^{DED2} domains to study amino acid variations in different taxonomic groups such as mammals, birds, and fishes (supplementary fig. S9, Supplementary Material online). For this, we analyzed the BPPS subfamily groups 67, 53, and 98, corresponding to mammal, bird, and fish sequences, respectively, and extracted the residue positions that corresponded to the mCASP8^{DED2} side of the mCASP8$^{DED2\text{-}DED1}$ interface. Mammals exclusively possess the F residue at the 122nd position, while in a few bird and ray-finned fish species, L and Y are present, respectively (supplementary fig. S9, Supplementary Material online). This raises the question: why do the residues at this position in mammals differ from those in fish and birds? To investigate the structural impact of differing residues at the 122nd position, we used computational mutagenesis to analyze the F122-Y8 positions (Fig. 4). Analysis of the CASP8 filament showed that type I residues are predominantly hydrophobic (Fu et al. 2016), as indicated by Eisenberg hydrophobic contour plots (Fig. 4), suggesting conservation of hydrophobicity at the 122nd position through evolution. We studied the impact of this residue variation further in the section "Mutation of evolutionarily related CASP8 residues causes disruption in the mCASP8^{DED} stability and oligomerization and mCASP8^{DED}-mASC^{PYD} interaction."

Key Interface Residues From mCASP8^{DED2} are Implicated in the mCASP8^{DED}-mASC^{PYD} Heterotypic Interaction

In the second component of our study, we investigated potential interactions within the mCASP8^{DED}-mASC^{PYD} complex interface using a residue coupling technique. We identified key interface residues from mCASP8^{DED2} (specifically, N168 and S170 through the BPPS method; supplementary fig. S5a, Supplementary Material online) but not from mCASP8^{DED1}. We applied the EVcouplings complex module (Hopf et al. 2019) using domain sequences and mapped the coupling patterns onto the superimposed model. Despite a significant number of effective sequences, EVcouplings did not detect clear correlated patterns at the interface (data not shown). Given the challenges with identifying interface residues through residue coupling analyses alone, we expanded our approach to include a combination of sequence- and structure-based methods. Using the superimposed complex model as the reference to identify the mCASP8^{DED}-mASC^{PYD} heterodomain interface, we first retrieved the ASC^{PYD} domain sequences captured in the BPPS subfamily node 37 spanning various chordate classes (mammals, birds, fishes, amphibians, and reptiles) (supplementary fig. S10, Supplementary Material online). We then identified the other domain (CASP8^{DED1} and CASP8^{DED2}) sequences from their respective BPPS family subgroups (DED1, node 2; DED2, node 38; supplementary fig. S11, Supplementary Material online). While many of the mammalian ASC^{PYD} interface residues exhibited limited residue variation, as indicated by the sequence logo (supplementary fig. S10, Supplementary Material online), some variations were observed in key residues such as R41, which is critical for pro-CASP8 binding, with substitutions such as L in birds and W in amphibians. Additionally, the interface ASC^{PYD} residues facing CASP8^{DED1} and CASP8^{DED2} tend to be hydrophobic, positively charged, and polar in nature (supplementary fig. S10, Supplementary Material online). Sequence logos of CASP8^{DED1} and CASP8^{DED2} interface facing ASC^{PYD} showed residues enriched in negatively charged and a blend of neutral and polar residues, respectively (supplementary fig. S11, Supplementary Material online). Furthermore, comparative protein models of select organisms from various chordate classes suggested charge complementarity at the CASP8^{DED}-ASC^{PYD} interface (supplementary fig. S12, Supplementary Material online). Additionally, the E12 residue of mCASP8^{DED1} and N168, K169, and S170 residues of mCASP8^{DED2} were highly conserved across various classes, which could indicate potential functional relevance.

Domain Interactions in the mCASP8^{DED}-mASC^{PYD} Complex From Dynamic Simulations

To improve the predictive power of our computational analyses, we conducted molecular dynamic simulations aimed at replicating protein physiology within cells and elucidating the role of interface residues identified by these methods. We used molecular dynamic simulations to assess stability (RMSD and R_g), flexibility (RMSF), hydrogen bonding, and binding free energy contributions of the mCASP8^{DED}-mASC^{PYD} complex. Given the oligomeric and filamentous nature of these complex models (supplementary figs. S13 and S14, Supplementary Material online), they exhibited stability in packing the characteristic 6 α-helical bundle, as indicated by the RMSD (root mean square deviation) measure, fluctuating around ~4 to 4.5 Å in both models (supplementary figs. S13a and S14a, Supplementary Material online). The R_g (radius of gyration) measure of docked and superimposed models fell within the range of 16 to 16.5 Å and 18.5 to 19.5 Å, respectively, suggest stable packing of the mASC^{PYD} layer upon the mCASP8^{DED} filament (supplementary figs. S13b and S14b, Supplementary Material online). Notably, the RMSF was higher in certain sequence windows for both models (supplementary figs. S13c and S14c, Supplementary Material online); specifically, in residue positions 51 to 61, corresponding to the surface-exposed region of mCASP8^{DED1}, and 125 to 135 of mCASP8^{DED2}, in the domain interface between mCASP8^{DED1} and mCASP8^{DED2}. We then examined the H-bond interactions of domain interface residues in the simulation trajectory. In the docked model, a nonpattern mCASP8^{DED2} residue, E154, developed extensive H-bonding with R38 of mASC^{PYD}. The pattern residue of mCASP8^{DED2}, E147, developed H-bonds with H32 of mCASP8^{DED1} (supplementary fig. S13d, Supplementary Material online). Within the heterodomain interface of the docked model, both E147 and E154 of mCASP8^{DED2} participated in creating an electronegative patch that complemented the electrostatic positive surface lined by the R38 and R41 residues of mASC^{PYD} (supplementary fig. S13e, Supplementary Material online). These potential electrostatic complementarity and H-bonding properties suggest that the residues (E147 and E154) are promising candidates for functional analyses in future studies to validate their roles.

Further analysis of the superimposed model trajectory showed persistent H-bonding of E12 and E13 of mCASP8^{DED1} with R38 and R41 residues of mASC^{PYD} (supplementary fig. S14d and e, Supplementary Material online), suggesting potential functional relevance. Similarly, the mCASP8^{DED2} interface residues, N168

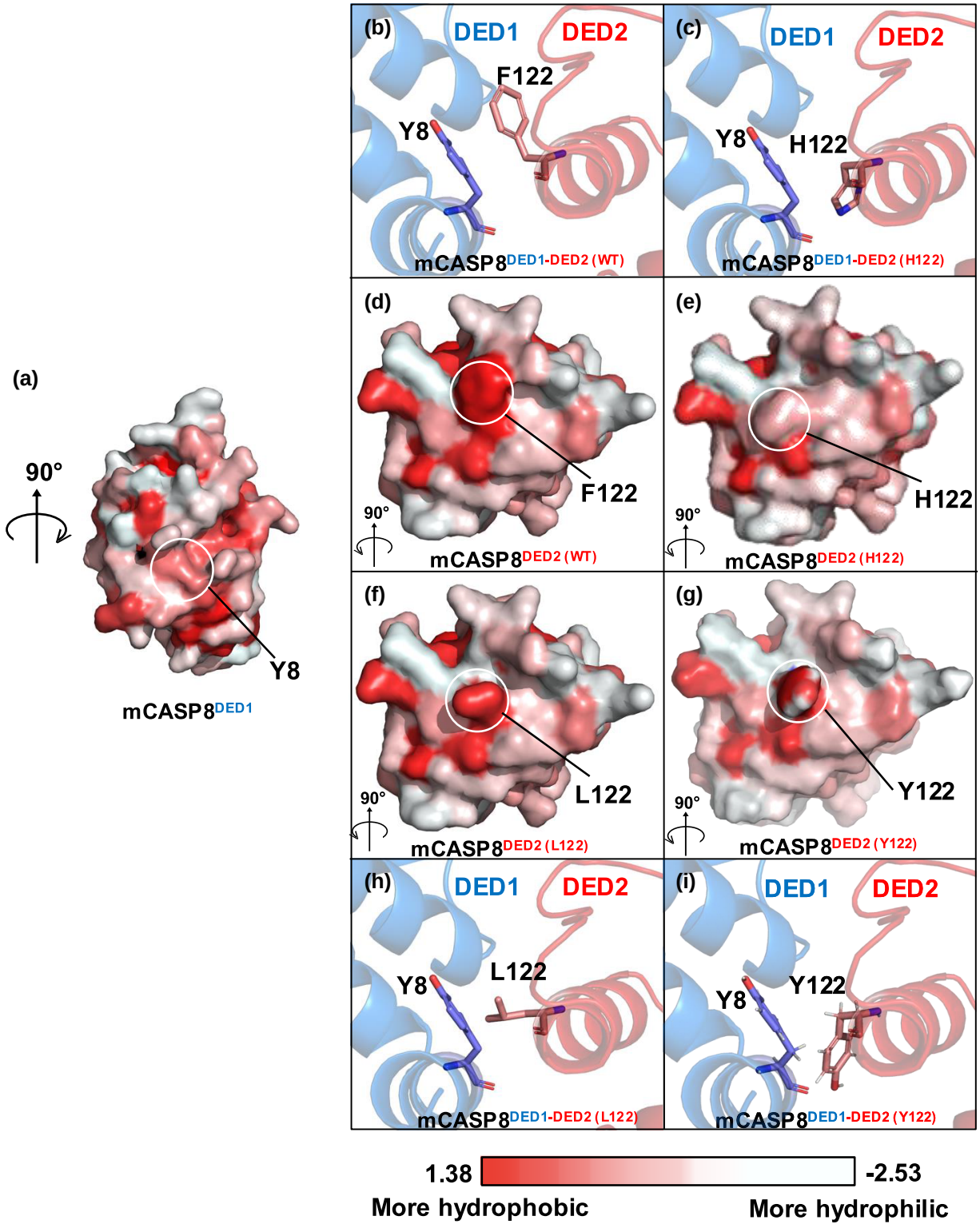

Fig. 4. Hydrophobic interface of mCASP8^{DED} filament. a–i) Close view of wild type mCASP8^{DED} (F122) and its mutants (H122, L122, and Y122). Within the mCASP8 filament, the F122 (b), H122 (c), L122 (h), and Y122 (i) residues (orange stick) of the DED2 domain close to the Y8 residue (blue stick) of the adjacent DED1 domain are shown in cartoon representation. Hydrophobicity potential mapped onto the accessible surface area of the mCASP8 structures (all rotated by 90°) is shown with residues F122 (d), H122 (e), L122 (f), and Y122 (g), and Y8 highlighted (a). Hydrophobicity potential was calculated using the Eisenberg hydrophobicity scale and rendered using the PyMOL program.

and K169, engaged in H-bonds with S58 and G35 residues of mASC^{PYD}, respectively (supplementary fig. S14d and e, Supplementary Material online). To gain deeper insights into whether these interface residues contributed to the free energy of mCASP8^{DEDs}-mASC^{PYD} binding, we analyzed the residue-wise energy decomposition in the superimposed model as well as comparative models built across different organisms spanning various chordate and nonchordate classes (supplementary fig.

S15, Supplementary Material online). The mCASP8^{DED1} interface residues E12 and E13, along with their equivalent residues in various protein models of different organisms, made substantial contributions to the total free energy of binding. Similarly, the N168, K169, and S170 residues of mCASP8^{DED2}, along with their equivalent positions in different organisms, displayed a relatively secondary contribution to binding energy if the residues were conserved. The major contribution of DED1 interface residues to binding free energy (supplementary fig. S15, Supplementary Material online) may be attributed to the close positioning of mCASP8^{DED1} residues to R41, a site of functional importance in mASC^{PYD} (Vajjhala et al. 2015). The DED residues in the heterotypic interface of the mCASP8^{DED}-mASC^{PYD} complex were compared with the pattern residues obtained from the superfamily analysis across different DED family members (supplementary fig. S16, Supplementary Material online). We observed that the pattern residues and the interface residues did not overlap for DED1 family members (supplemenatry fig. S16a, Supplementary Material online). In contrast, some of the pattern residues of mCASP8^{DED2} overlapped with those of other DED2 family members (supplementary fig. S16b, Supplementary Material online), such as chicken CASP18a and rainbow trout CASP10a (supplementary fig. S5b, Supplementary Material online), and they were present in the interface. Furthermore, we mapped the pattern residues identified by BPPS (superfamily) and DARC (query-based) methods, along with positively selected sites from the site-specific positive selection analysis, to evaluate the congruity among these residues with experimentally tested mutants of the hCASP8 filament. While some pattern residues of mCASP8^{DED2} (supplementary fig. S17, Supplementary Material online), including F122, L123, C131, and R149, were previously characterized in terms of hCASP8 filament stability, none of these residues fall within the heterotypic interface of the mCASP8^{DED}-mASC^{PYD} complex. Additionally, although the positively selected sites (supplementary fig. S6, Supplementary Material online) do not overlap with the pattern residues, their proximity to pattern residues (supplementary fig. S17, Supplementary Material online) may affect the physicochemical properties of the CASP8-ASC heterotypic interface and possibly alter molecular interactions. The absence of pattern residues in the heterotypic interface might reflect rapid evolution driven by adaptation at, for example, the species or subspecies level, and thereby requiring direct coupling analyses (DCA) across heteromeric subunits (Reed et al. 2004; Neuwald and Altschul 2016).

Mutation of Evolutionarily Related CASP8 Residues Causes Disruption in the mCASP8^{DED} Stability and Oligomerization and mCASP8^{DED}-mASC^{PYD} Interaction

Our analyses using the DARC method identified residues with likely roles in mCASP8^{DED} filament stability and oligomerization. Therefore, we mutated the F122 residue, the most-constrained residue in the mCASP8^{DED2}, to determine its functional relevance. Negative staining showed disruption of the mCASP8^{DED} filament with both the F122E (complete disruption) and F122H (partial disruption) mutations (Fig. 5), providing a proof of concept to validate that our computational analysis identified residues that are critical for filament formation. Sequence analysis across phylogenetic classes showed that F122 is predominantly selected through evolution (supplementary fig. S9, Supplementary Material online). Mutating this residue to E122 was previously shown to abrogate the hCASP8^{DED} filament (Fu et al. 2016). Previous mutagenesis data on the ASC filament (e.g. Y187 to H187) (Li et al. 2018) indicates that mutating to H in place of a hydrophobic residue partially disrupts filament formation. This suggests that F122 is highly selected through evolution to grow and stabilize the CASP8^{DED} filament.

We further sought to determine whether the residues identified through our computational approach affected the CASP8-ASC interaction. To test this, we performed a charge reversal mutation of E147, the pattern residue of mCASP8^{DED2} located at the heterotypic interface (supplementary fig. S7a, Supplementary Material online), to R147. However, this E147R mutation did not disrupt the mASC^{PYD}-mCASP8^{DED} interaction (supplementary fig. S18, Supplementary Material online). Additionally, we mutated the E154 residue, which forms extensive hydrogen bonding with the R38 residue of mASC^{PYD} at the heterotypic interface (supplementary fig. S13d, Supplementary Material online). The E154D mutation also did not reduce the mASC^{PYD}-mCASP8^{DED} interaction (supplementary fig. S18, Supplementary Material online). Based on these results, we hypothesized that mutating a single residue may not be sufficient to disrupt the binding, while mutating the most relevant residues together from at least 1 domain of mCASP8^{DED} in the heterotypic interface might affect mCASP8^{DED}-mASC^{PYD} complex formation. Indeed, we found that including both the E147R and E154D mutations together resulted in a partial reduction in the mASC^{PYD}-mCASP8^{DED} interaction (supplementary fig. S18, Supplementary Material online), although it was not completely abrogated. This observation suggests that additional interacting residues, potentially also including residues in mASC^{PYD}, may also play a role. These results suggest that mammalian CASP8^{DED} and ASC^{PYD} have complementary molecular properties enabling their molecular association. Together, these in vitro analyses confirm that the residues identified in our computational analyses have a functional role in the critical CASP8 activities that drive complex formation and subsequent cell death.

Conclusion

CASP8, a key component of the metazoan molecular toolkit and PANoptosome, can drive nonlytic apoptosis and lytic PANoptosis, as demonstrated by numerous genetic, biochemical, and microscopy experiments (Boldin et al. 1996; Muzio et al. 1996; Sakamaki et al. 2014; Kuriakose et al. 2016; Christgen et al. 2020; Kesavardhana et al. 2020; Malireddi et al. 2020; Zheng et al. 2020; Karki, Sharma et al. 2021; Karki, Sundaram et al. 2021; Lee et al. 2021; Karki et al. 2022; Wang et al. 2022; Chen et al. 2023; Sundaram et al. 2023, 2024; Sharma et al. 2025). Here, we decoded the heterotypic interaction between mCASP8^{DED} and mASC^{PYD}, identifying key evolutionarily conserved residues that are crucial for CASP8 oligomerization and the CASP8-ASC interaction. The hierarchical tree structure of DD superfamily members effectively distinguished various members such as CARD, DED, and PYD into subgroups based on shared or diverse evolutionary and functional relationships, with similar groupings noted across mammalian CASP phylogenetic clades (Sakata et al. 2007; Eckhart et al. 2008; Sakamaki and Satou 2009; Sakamaki et al. 2014).

Further, the homotypic traits among subfamily members captured at the tree family level (e.g. CASP8^{DED1}-FADD^{DED}, NLRP3^{PYD}-ASC^{PYD}) suggest the presence of key molecular associations crucial to the formation of inflammasomes and

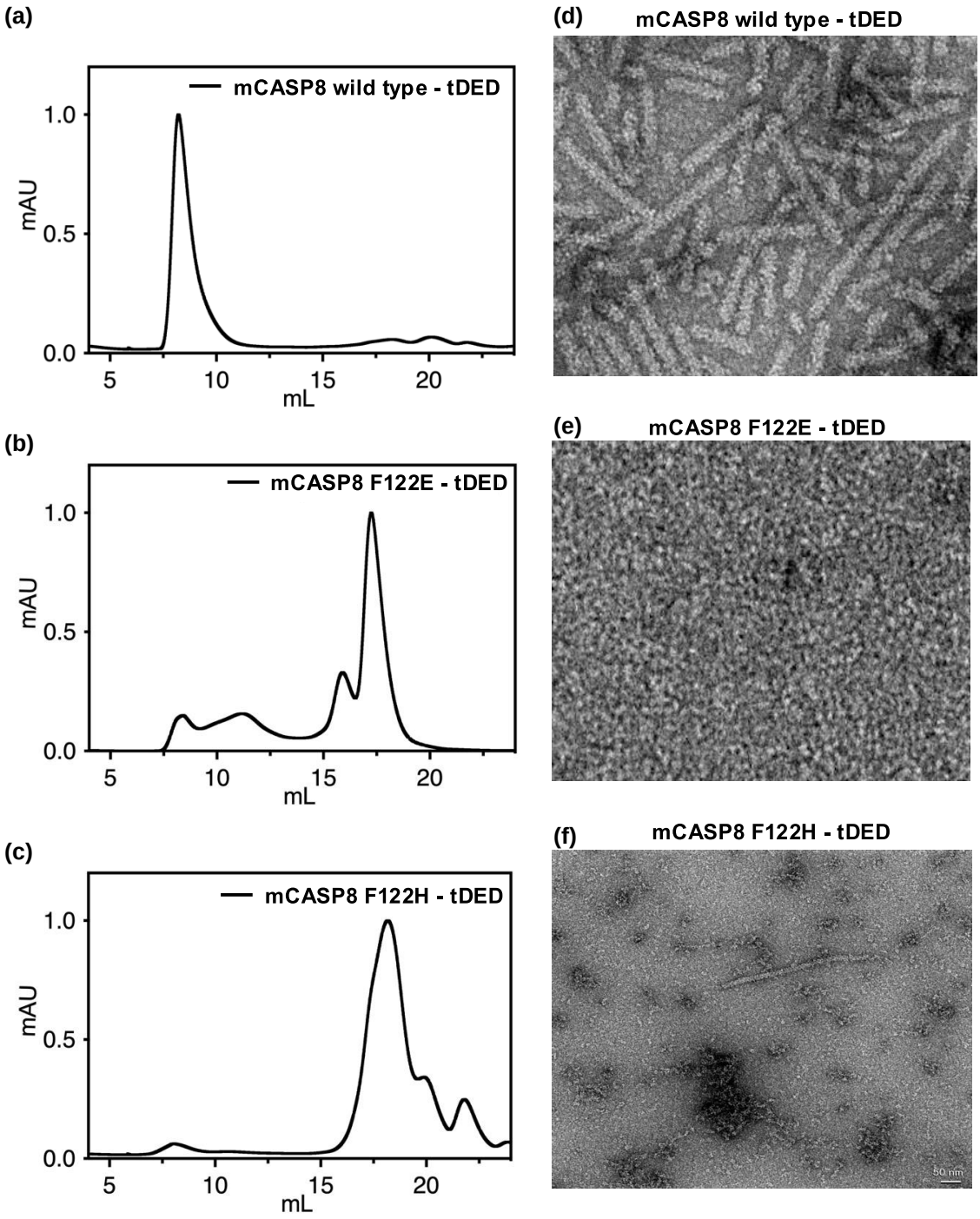

Fig. 5. Mutation of key CASP8^{DED} residues disrupts filament formation. a–c) Size exclusion chromatography (SEC) profiles of mCASP8^{DED} wild type (a) and mutants (E122 (b) and H122 (c)). d–f) Negative staining micrographs of mCASP8^{DED} wild type (d) and mutants (E122 (e) and H122 (f)).

certain PANoptosomes (Christgen et al. 2020; Malireddi et al. 2020; Zheng et al. 2020; Lee et al. 2021; Sundaram et al. 2023, 2024; Sharma et al. 2025). The tree also captured key events in caspase evolution, including the fish-specific CASP8^{DED2} subgroup, which reflects adaptations from chromosomal rearrangements in the teleost lineage (Sakata et al. 2007; Spead et al. 2018). These insights from the hierarchical tree contribute to a deeper understanding of the molecular mechanisms of the death family members underlying immune responses and their evolutionary significance. Our findings highlight the evolutionary adaptations of DED and PYD in CASP8 and ASC and their potential roles in PANoptosome formation.

The search for mASC homologs identified protein sequences exclusively in chordates, except for most of the birds, consistent with previous genome analyses (Billman et al. 2024). This suggests a recent evolutionary development with specialized functions, such as the inflammasome and PANoptosome adaptor roles. CASPs, including CASP8, have existed since the early Cambrian period (~520 MYA) (Sakamaki et al. 2015) and are present in all eukaryotes and their ancestral mitochondrial endosymbionts (Koonin and Aravind 2002).

CASP8, shaped by evolutionary pressures, underwent gene duplication early in vertebrate evolution, leading to paralogs such as CASP10, FADD, and cFLIP (Eckhart et al. 2008; Sakamaki and Satou 2009; Sakamaki et al. 2015). Different vertebrate lineages followed distinct evolutionary paths, with rodents losing CASP10 and teleosts gaining novel CARD-containing CASP8 through chromosomal rearrangements (Sakata et al. 2007; Eckhart et al. 2008; Sakamaki and Satou 2009; Spead et al. 2018). ASC, emerging later in the Jurassic period (~201 MYA) (Brusatte et al. 2015), coincided with the divergence of birds from reptiles (Billman et al. 2024), suggesting the CASP8-ASC interplay is a relatively recent evolutionary development. Consequently, PANoptosis, driven by this interaction, is a newly emerged inflammatory pathway, likely exclusive to mammals, validated in human and mouse models to drive inflammation and disease.

Overall, our findings suggest a unique evolutionary adaptation of CASP8 to interact with ASC, potentially leading to PANoptosome formation and performing redundant functions with CASP1, which can contribute to IL-1β–mediated inflammatory diseases. Future functional studies will be needed to fully understand the specific residues that are critical for diverse CASP functions, and this study provides evolutionary information to aid in the characterization of mutant phenotypes. Together, these evolutionary insights have implications for understanding mammalian immune responses and developing therapeutic strategies for inflammatory diseases.

Materials and Methods

MSA of DD Superfamily

Domain family hierarchy was analyzed for the DD superfamily, which is a group of related domains with common ancestry, a set of conserved residues, and a shared primary function (Neuwald 2014b; Neuwald et al. 2018). The domain hierarchy is presented as a hierarchical multiple sequence alignment (hiMSA), a set of MSAs organized hierarchically, depicting individual subgroups (sets of closely related protein sequences) within a superfamily (ftp://ftp.ncbi.nlm.nih.gov/pub/mmdb/cdd/hiMSA) (Wang et al. 2023). Further, template MSA files was used to guide the global alignment of each subgroup MSA against other subgroup MSAs within the same superfamily (Neuwald and Altschul 2016; Neuwald et al. 2020). The hiMSA of the DD superfamily (cd08304), consisting of 63 leaf nodes representing different subgroups, was converted to MAPGAP's input files using the CDD2MGS program (Neuwald 2009; Neuwald et al. 2020). In parallel, 93,105 protein sequences of the DD superfamily (IPR011029; as of 09/14/2022) belonging to the animal kingdom were retrieved from the InterPro database (Paysan-Lafosse et al. 2023) and were annotated with taxonomic ranks (phylum and kingdom) using the AddPhylum program (Neuwald et al. 2020) (sequence alignment with accession IDs is included in the supplementary data, Supplementary Material online file). The MAPGAPS program v2.1 was used to align the annotated protein sequences against the superfamily hiMSA using the template MSA, creating an MSA in collinear multiple alignment format (Neuwald 2009; Neuwald et al. 2020). The PurgeMSA program (Neuwald et al. 2020) was used to remove all but 1 sequence among those sharing ≥80% sequence identity, resulting in a final MSA of 21,714 protein sequences. We then supplemented the final MSA with 79 experimentally resolved 3D protein structures (X-ray and cryo-EM structures; obtained from MAPGAPS search against the NCBI pdbaa database, accessed 2022 September 22) and 8 AlphaFold models (Jumper et al. 2021) when experimental structures were unavailable. The full-length AlphaFold models were obtained from the AlphaFold Protein Structure Database (https://alphafold.ebi.ac.uk) (Varadi et al. 2024) hosted by the European Bioinformatics Institute. Full-length protein models were downloaded, and death fold regions were extracted and used as inputs for BPPS and DARC calculations. Hydrogen (H) atoms were added to the protein structures using the REDUCE program v3 (Richardson 2024).

Superfamily Analysis of DD

Superfamily analysis of the DD was performed using the BPPS program v1.1 (Neuwald et al. 2018). BPPS models the evolutionary process wherein homologous proteins within a superfamily, characterized by a common structural core, often undergo divergence, resulting in the formation of subgroups that serve distinct functional roles. At the sequence level, such functional divergence can be identified through correlations among residue patterns distinct to each subgroup. These correlations likely arise from structural and biochemical constraints, offering insights into protein properties crucial for functional specificity. Utilizing Markov chain Monte Carlo (MCMC) sampling, BPPS partitions the input MSA into hierarchically arranged subgroups based on correlated residue patterns unique to each subgroup. This generates a set of hierarchically arranged "contrast alignments," one for each subgroup (Neuwald 2014a; Neuwald et al. 2018) along with corresponding PyMOL scripts (Schrödinger 2024a) that map pattern residues onto protein structures. Each contrast alignment consists of an aligned set of "foreground" sequences harboring a set of pattern residues that distinguish them from a set of background sequences, namely the most closely related sequences that have diverged from the foreground sequences. For each pattern position, the MCMC sampler computes the LPR of the observed foreground residues that have been generated by a statistical model based on the foreground versus the background residue frequencies; this measures the degree to which the foreground residues have diverged from (or contrast with) the background residues at that position (Neuwald et al. 2018, 2022; Tondnevis et al. 2020). The LPR measures the information (in nats) encoded by each subgroup's foreground sequences reflecting the selective pressure imposed at pattern positions (Neuwald and Altschul 2016; Neuwald et al. 2022). The BPPS program built a tree of DD MSA with 122 nodes with a depth of 3, consisting of a single superfamily, 26 families (nodes), and 95 subfamilies (sub-nodes).

In addition, a phylogenetic tree of CASP N-terminal domains (CARD and DED) was reconstructed using IQTREE2 software (Minh et al. 2020). CASP N-terminal domain sequences were extracted from above curated InterPro dataset (Paysan-Lafosse et al. 2023), filtered for redundancy, and then aligned using MAFFT program v7 (Katoh et al. 2019). JTT + G4 was selected as the best substitution model, and *C. elegans* ced-3 CARD domain sequence was chosen as the outgroup. The tree was built with 1,000 ultrafast bootstrapping replicates and annotated using IROKI program (Moore et al. 2020).

Site-specific Positive Selection Analysis of CASP8^{DED2} Domain

Site-specific positive selection analysis of CASP8^{DED2} orthologs was performed using the FUBAR (Fast, Unconstrained

Bayesian AppRoximation for Inferring Selection) program (Murrell et al. 2013). Initially, CASP8 orthologs were retrieved from the NCBI Gene database (Sayers et al. 2024), filtered for redundancy, and then aligned using MAFFT program v7 (Katoh et al. 2019) with the curated $CASP8^{DED2}$ coding regions of human and mouse as templates. This resulted in a final sequence set of 236 sequences and 71 sites.

Deep Analysis of DDs Using Residue Coupling and Statistical Inference Models

Unlike the BPPS method, which partitions the input MSA into multiple subgroups, the DARC method's first step involves partitioning the input MSA by identifying the query sequence within it, creating 1 or more subgroups that include the query sequence (Tondnevis et al. 2020). The focus here is on the query's lineage within the superfamily hierarchy, achieved by initially defining the query's family through residue patterns that effectively differentiate family members from other superfamily members. These patterns are often linked to constraints on residues within the query sequence's lineage, presumably influencing functional specificity. The DARC (v0.6) program also investigates evolutionary relationships within protein multimeric complexes using an input MSAs for each subunit (Neuwald and Altschul 2018; Tondnevis et al. 2020). It recognizes query sequences in each MSA to determine residue patterns that may be localized to the protein complex interface. The mouse $CASP8^{DED}$ domain (DED1 and DED2 domains were submitted separately in each calculation), and mouse ASC^{PYD} domain sequences are used as queries in 2 MSAs, DD MSA and ASC MSA. For the ASC MSA, a jackhmmer (Eddy 2011) search of the mouse full-length ASC sequence was performed for 5 iterations using the default settings. Sequence hits containing PYD and CARD domains were analyzed, and alignment was performed using MAPGAPS program (Neuwald 2009; Neuwald et al. 2020). The second step of DARC involves DCA using the CCMpred program v1 (Seemayer et al. 2014) to predict structural contacts between columns within the query family's subalignment. This prediction is based on the identification of coevolving residue pairs across aligned sequences, where directly correlated mutations suggest potential physical interactions between residues in the protein's 3D structure. Amino acid residue changes at a given position are typically compensated by changes at another interacting position in the input MSA, maintaining structural integrity and forming the basis for DCA (Neuwald et al. 2022). DARC, through initial cluster analysis, calculates the statistical significance (S; $-\log_{10}[P\text{-value}]$) of the correspondence between pattern residues and 3D contacts ($_{3D}S_p$), DC scores and 3D contacts ($_{3D}S_{DC}$), and pattern residues and DC scores ($_{DC}S_p$). DARC created a PyMOL session (Schrödinger 2024a) file that maps pattern residues and DC pairs onto protein structures postcalculation, which was manually edited to show only results that overlapped the top 10 pattern residues (ranked by their contributions to the LPR in nats) and the residues in the DC pair.

Models of $mCASP8^{DED}$-$mASC^{PYD}$ Filament

Based on the cryo-EM structure of the hCASP8 tandem DED filament (PDB: 5l08; resolution: 4.60 Å) (Fu et al. 2016), a homology model for the mCASP8 filament was built using the MODELLER package v10.5 (Šali and Blundell 1993). The DED sequences of human and mouse CASP8 share 63.6% identity and 76.1% similarity. The best model identified through DOPE statistical potential, exhibits closely aligned energy profiles with the template, indicating the model's accuracy. Additionally, Ramachandran's stereochemistry check, with 96.1% favorable geometry in the $mCASP8^{DED}$ core region, further supports the model's accuracy. Subsequently, the $mCASP8^{DED}$-$mASC^{PYD}$ complex was developed by site-directed docking of the $mASC^{PYD}$ monomer (PDB: 2n1f; resolution: 4.00 Å) (Sborgi et al. 2015) onto the modeled $mCASP8^{DED1\text{-}DED2}$ interface using the HADDOCK program (academic version 2.2) (van Zundert et al. 2016). The constraints for docking included R41 of ASC^{PYD} and F143 of $CASP8^{DED}$; R41A mutation of $hASC^{PYD}$ affects procaspase-8 binding (Vajjhala et al. 2015); the DED interfacial residue F143 of mCASP8 was chosen, as both DED domains of CASP8 are required for ASC^{PYD} binding (Vajjhala et al. 2015). Another model of the $mCASP8^{DED}$-$mASC^{PYD}$ complex was built by superimposing the $mASC^{PYD}$ monomers (RMSD: 0.131 Å) onto the top layer of $mCASP8^{DED}$ filament using the MM-align program (Mukherjee and Zhang 2009). The $mCASP8^{DED}$-$mASC^{PYD}$ model was also predicted using AlphaFold2 multimer (Evans et al. 2022)/ColabFold (Mirdita et al. 2022). Protein structures were energy-minimized using GROMACS MPI v2021.2 (Abraham et al. 2015) with the OPLS all-atom force field (Jorgensen et al. 1996). Structures were positioned in a cubic box with periodic boundary conditions (enabled a minimum distance of 1 nm from the box edges) and solvated using single point charge (SPC) water model. The system was neutralized by adding counterions and energy-minimized using the steepest gradient technique with 1,00,000 steps until the maximum force on each atom was below 1,000 kJ/mol/nm. The HawkDock program v1 (Weng et al. 2019) was utilized to calculate the binding free energy and per-residue energy decompositions of $CASP8^{DED}$-ASC^{PYD} models from diverse organisms using the MM/GBSA (molecular mechanics/generalized Born surface area) method. $CASP8^{DED}$ domains were defined as the receptor, and the ASC^{PYD} domain was defined as the ligand. The MM and electrostatics were computed using a polarizable force field based on the restrained electrostatic potential (ff02) (Cieplak et al. 2001) and a modified GB^{OBC} solvation model (Onufriev et al. 2004), with all other parameters set to default.

Dynamic Simulation of $mCASP8^{DED}$-$mASC^{PYD}$ Filament

The $mCASP8^{DED}$-$mASC^{PYD}$ filament was simulated over a 500 ns time scale using the DESMOND module of the Schrödinger suite 2023-1 (Bowers et al. 2006; Schrödinger 2024b). Initially, the filament was prepared with the Protein Preparation Wizard (Schrödinger 2024c), involving atom-typing with the OPLS4 force field (Lu et al. 2021), assigning bond orders and protonation states (pH 7.0), adding hydrogen atoms, and optimizing hydrogen bond networks. Furthermore, restrained energy minimization was performed with an RMSD convergence of heavy atoms set at 0.30 Å. An orthorhombic box enclosing the filament was created using the System Builder module, solvated with the SPC water model, and neutralized by adding Na^+ ions. Following equilibration, an unrestrained production run with the NPT (constant number of atoms, pressure, and temperature) ensemble at 300 K temperature and 1.01325 bar pressure was conducted. The system was monitored using the Nose-Hoover thermostat (1 ps relaxation time) and the isotropic Martyna-Tobias-Klein barostat (2 ps

relaxation time). Coulombic interactions, both short- and long-range, were handled using the cutoff method (9 Å cutoff radius) and the smooth particle mesh Ewald method (Darden et al. 1993) with the RESPA integrator (Tuckerman et al. 1992), respectively. Frames from the system trajectory were exported at 2 ps intervals for subsequent analysis, employing metrics such as RMSD (root mean square deviation), RMSF (root mean square fluctuation), and Rg (radius of gyration). Protein interactions and domain interfaces were analyzed using the PDBePISA webserver (Krissinel and Henrick 2007; Protein Data Bank in Europe 2024).

Sequence and Structure Representations

MSAs were generated using Clustal Omega program (Madeira et al. 2024) with default settings and rendered using WebLogo v3.0 (Crooks et al. 2004) and ESPript3 (Robert and Gouet 2014) utilities. Electrostatic surface potentials of protein structures were computed using the linear Poisson-Boltzmann equation in the DelPhi webserver (Smith et al. 2012). Initially, mCASP8^{DED}-mASC^{PYD} was converted to PQR format by assigning titration states and atomic charges (pH 7.0) based on the AMBER force field (Ponder and Case 2003). Electrostatics were then calculated at grid points with a 1.0 Å resolution, 0.15 salt concentration, and a 1.4 Å probe radius, with internal and external dielectric constants of 4 and 80, respectively. Hydrophobicity potentials were calculated upon the accessible surface area of mCASP8^{DED}-mASC^{PYD} using Eisenberg hydrophobicity scale (Eisenberg et al. 1984). Structure illustrations were generated using PyMOL software (Schrödinger 2024a). Animal icons were obtained from BioRender. All high-end calculations were done in the St. Jude High Performance Computing facility (HPCF).

Cloning, Expression, and Purification of CASP8^{tDED} and ASC^{PYD}, and Negative Staining of CASP8^{tDED}

CASP8^{tDED} and ASC^{PYD} were cloned into a modified pET28 vector containing His-MBP as an N-terminal tag. These clones were then transformed into BL21 (DE3) *E. coli* cells, which were grown at 37 °C in LB medium supplemented with 50 mg/mL kanamycin until the culture reached an optical density of ~0.8. The proteins were overexpressed by adding IPTG to a final concentration of 0.5 mM. After an additional incubation period of 8 h at 18 °C, the culture was harvested by centrifugation at 4,500 x *g* for 30 min and stored at −80 °C. Cell pellets from both His-MBP-CASP8^{tDED} and His-MBP-ASC^{PYD}, totaling 2 L of culture each, were resuspended in 100 mL of buffer-A (50 mM Tris buffer, pH 8.0; 500 mM NaCl; 10% glycerol; 10 mM βME). The suspensions were lysed through sonication and centrifuged at 45,000 x *g* at 4 °C for 30 min. The supernatants were then loaded onto a nickel affinity column pre-equilibrated with buffer-A. The proteins were eluted with buffer-B (50 mM Tris buffer, pH 8.0; 150 mM NaCl; 500 mM imidazole). The purified samples for CASP8^{tDED} were visualized using a negative staining electron microscope.

Fractions containing His-MBP-ASC^{PYD} were pooled and treated with 2 mg of HRV-3C protease per 20 mg of His-MBP-ASC^{PYD}, then incubated overnight at 4 °C while dialyzing in parallel to remove excess imidazole from the elution buffer. The digested proteins were centrifuged at 4,500 x *g* for 20 min to separate HRV3C protease aggregates. Immobilized metal affinity chromatography (IMAC) was used to further fractionate the cleaved proteins, and the cleaved ASC-containing flow-through was subsequently concentrated to 1 mg/mL. His-MBP-CASP8^{tDED} and ASC^{PYD} were further purified using size exclusion chromatography (Superdex 200 HR 10/300 increase) (GE Healthcare), which was pre-equilibrated with 20 mM Tris, pH 7.5; 150 mM NaCl; 2 mM TCEP.

CASP8^{tDED} and ASC^{PYD} Pull Down Assays

Initially, 20 µM His-MBP-CASP8^{tDED} was used as a bait and incubated with 200 µL of prewashed Ni-NTA beads in a buffer containing 20 mM Tris pH 7.5, 150 mM NaCl, 2 mM TCEP for 1 h at 4 °C. After washing the beads with 40 column volumes of the same buffer, the Ni-NTA beads were incubated with 30 µM ASC^{PYD} for an additional 1 h at 4 °C. Finally, the beads were washed with an additional 40 column volumes, and the Ni-NTA-bound proteins were mixed with 50 µL of 2× sample solubilizing buffer, boiled at 98 °C for 5 min, and analyzed using SDS-PAGE.

Supplementary Material

Supplementary material is available at *Molecular Biology and Evolution* online.

Acknowledgments

We thank all the members of the Kanneganti laboratory for their comments and suggestions during the development of this manuscript. We also thank R. Tweedell, PhD, for scientific editing and writing support, and S. Resende, PhD, for scientific editing support. We thank Chad Burdyshaw, St. Jude HPCF, for help in computing resource allocations.

Author Contributions

Sivakumar Prasanth Kumar (Conceptualization, Methodology, Computational experiments, Data interpretation, Writing—manuscript), Andrew F. Neuwald (Conceptualization, Methodology, Computational experiments, Data interpretation), Thirumala-Devi Kanneganti (Conceptualization, Data interpretation, Funding, Supervision), Raghvendra Mall (Computational experiments), Eswar Kumar Nadendla (Negative staining microscopy, Protein purification, Pull down assays), Syed Asfarul Haque (Negative staining microscopy), and R.K. Subbarao Malireddi (Data interpretation)

Funding

Work from our laboratory is supported by the US National Institutes of Health (AI101935, AI124346, AI160179, AR056296, and CA253095 to T.-D.K.) and the American Lebanese Syrian Associated Charities (to T.-D.K.). The content is solely the responsibility of the authors and does not necessarily represent the official views of the National Institutes of Health.

Conflict of Interest

The authors declare no competing interests.

Data Availability

All datasets were derived from sources in the public domain with the relevant accessions mentioned in the article. The data and analysis underlying this article are available in the article and in its online supplementary material.

References

Abraham MJ, Murtola T, Schulz R, Páll S, Smith JC, Hess B, Lindahl E. GROMACS: high performance molecular simulations through multi-level parallelism from laptops to supercomputers. *SoftwareX*. 2015:1-2:19–25. https://doi.org/10.1016/j.softx.2015.06.001.

Andreeva L, David L, Rawson S, Shen C, Pasricha T, Pelegrin P, Wu H. NLRP3 cages revealed by full-length mouse NLRP3 structure control pathway activation. *Cell*. 2021:184(26):6299. https://doi.org/10.1016/j.cell.2021.11.011.

Aravind L, Dixit VM, Koonin EV. Apoptotic molecular machinery: vastly increased complexity in vertebrates revealed by genome comparisons. *Science*. 2001:291(5507):1279–1284. https://doi.org/10.1126/science.291.5507.1279.

Billman ZP, Hancks DC, Miao EA. Unanticipated loss of inflammasomes in birds. *Genome Biol Evol*. 2024:16(7):evae138. https://doi.org/10.1093/gbe/evae138.

Boldin MP, Goncharov TM, Goltsev YV, Wallach D. Involvement of MACH, a novel MORT1/FADD-interacting protease, in Fas/APO-1- and TNF receptor-induced cell death. *Cell*. 1996:85(6):803–815. https://doi.org/10.1016/S0092-8674(00)81265-9.

Bowers KJ, Chow E, Xu H, Dror RO, Eastwood MP, Gregersen BA, Klepeis JL, Kolossvary I, Moraes MA, Sacerdoti FD, *et al.* Scalable algorithms for molecular dynamics simulations on commodity clusters. In: Proceedings of the 2006 ACM/IEEE conference on supercomputing. Tampa, (FL): Association for Computing Machinery; 2006. p. 84.

Brusatte SL, O'Connor JK, Jarvis ED. The origin and diversification of birds. *Curr Biol*. 2015:25(19):R888–R898. https://doi.org/10.1016/j.cub.2015.08.003.

Chen W, Gullett JM, Tweedell RE, Kanneganti TD. Innate immune inflammatory cell death: PANoptosis and PANoptosomes in host defense and disease. *Eur J Immunol*. 2023:53(11):e2250235. https://doi.org/10.1002/eji.202250235.

Chinnaiyan AM, O'Rourke K, Tewari M, Dixit VM. FADD, a novel death domain-containing protein, interacts with the death domain of Fas and initiates apoptosis. *Cell*. 1995:81(4):505–512. https://doi.org/10.1016/0092-8674(95)90071-3.

Christgen S, Zheng M, Kesavardhana S, Karki R, Malireddi RKS, Banoth B, Place DE, Briard B, Sharma BR, Tuladhar S, *et al.* Identification of the PANoptosome: a molecular platform triggering pyroptosis, apoptosis, and necroptosis (PANoptosis). *Front Cell Infect Microbiol*. 2020:10:237. https://doi.org/10.3389/fcimb.2020.00237.

Cieplak P, Caldwell J, Kollman P. Molecular mechanical models for organic and biological systems going beyond the atom centered two body additive approximation: aqueous solution free energies of methanol and N-methyl acetamide, nucleic acid base, and amide hydrogen bonding and chloroform/water partition coefficients of the nucleic acid bases. *J Comput Chem*. 2001:22:1048–1057. https://doi.org/10.1002/jcc.1065

Crooks GE, Hon G, Chandonia JM, Brenner SE. WebLogo: a sequence logo generator. *Genome Res*. 2004:14(6):1188–1190. https://doi.org/10.1101/gr.849004.

Darden T, York D, Pedersen L. Particle mesh Ewald - an N.Log(N) method for Ewald sums in large systems. *J Chem Phys*. 1993:98(12):10089–10092. https://doi.org/10.1063/1.464397.

Daugherty MD, Malik HS. Rules of engagement: molecular insights from host-virus arms races. *Annu Rev Genet*. 2012:46(1):677–700. https://doi.org/10.1146/annurev-genet-110711-155522.

Dick MS, Sborgi L, Rühl S, Hiller S, Broz P. ASC filament formation serves as a signal amplification mechanism for inflammasomes. *Nat Commun*. 2016:7(1):11929. https://doi.org/10.1038/ncomms11929.

Eckhart L, Ballaun C, Hermann M, VandeBerg JL, Sipos W, Uthman A, Fischer H, Tschachler E. Identification of novel mammalian caspases reveals an important role of gene loss in shaping the human caspase repertoire. *Mol Biol Evol*. 2008:25(5):831–841. https://doi.org/10.1093/molbev/msn012.

Eddy SR. Accelerated profile HMM searches. *PLoS Comput Biol*. 2011:7(10):e1002195. https://doi.org/10.1371/journal.pcbi.1002195.

Eisenberg D, Weiss RM, Terwilliger TC. The hydrophobic moment detects periodicity in protein hydrophobicity. *Proc Natl Acad Sci USA-Biol Sci*. 1984:81(1):140–144. https://doi.org/10.1073/pnas.81.1.140.

Evans R, O'Neill M, Pritzel A, Antropova N, Senior A, Green T, Žídek A, Bates R, Blackwell S, Yim J, *et al.* Protein complex prediction with AlphaFold-Multimer. bioRxiv 463034. https://doi.org/10.1101/2021.10.04.463034, 10 March 2022, preprint: not peer reviewed.

Ferrao R, Wu H. Helical assembly in the death domain (DD) superfamily. *Curr Opin Struct Biol*. 2012:22(2):241–247. https://doi.org/10.1016/j.sbi.2012.02.006.

Fischer U, Stroh C, Schulze-Osthoff K. Unique and overlapping substrate specificities of caspase-8 and caspase-10. *Oncogene*. 2006:25(1):152–159. https://doi.org/10.1038/sj.onc.1209015.

Fu TM, Li Y, Lu A, Li ZL, Vajjhala PR, Cruz AC, Srivastava DB, DiMaio F, Penczek PA, Siegel RM, *et al.* Cryo-EM structure of Caspase-8 tandem DED filament reveals assembly and regulation mechanisms of the death-inducing signaling Complex. *Mol Cell*. 2016:64(2):236–250. https://doi.org/10.1016/j.molcel.2016.09.009.

Gurung P, Anand PK, Malireddi RK, Vande Walle L, Van Opdenbosch N, Dillon CP, Weinlich R, Green DR, Lamkanfi M, Kanneganti TD. FADD and caspase-8 mediate priming and activation of the canonical and noncanonical Nlrp3 inflammasomes. *J Immunol*. 2014:192(4):1835–1846. https://doi.org/10.4049/jimmunol.1302839.

Gurung P, Burton A, Kanneganti T-D. NLRP3 inflammasome plays a redundant role with caspase 8 to promote IL-1β–mediated osteomyelitis. *Proc Natl Acad Sci U S A*. 2016:113:4452–4457. https://doi.org/10.1073/pnas.1601636113.

Hofmann K. The evolutionary origins of programmed cell death signaling. *Cold Spring Harb Perspect Biol*. 2020:12(9):a036442. https://doi.org/10.1101/cshperspect.a036442.

Holland M, Rutkowski R, Levin TC. Evolutionary dynamics of proinflammatory caspases in primates and rodents. *Mol Biol Evol*. 2024:41(12):msae220. https://doi.org/10.1093/molbev/msae220.

Hollingsworth LR, David L, Li Y, Griswold AR, Ruan J, Sharif H, Fontana P, Orth-He EL, Fu TM, Bachovchin DA, *et al.* Mechanism of filament formation in UPA-promoted CARD8 and NLRP1 inflammasomes. *Nat Commun*. 2021:12(1):189. https://doi.org/10.1038/s41467-020-20320-y.

Hopf TA, Green AG, Schubert B, Mersmann S, Scharfe CPI, Ingraham JB, Toth-Petroczy A, Brock K, Riesselman AJ, Palmedo P, *et al.* The EVcouplings Python framework for coevolutionary sequence analysis. *Bioinformatics*. 2019:35(9):1582–1584. https://doi.org/10.1093/bioinformatics/bty862.

Horowitz LB, Shaham S. Apoptotic and nonapoptotic cell death in *Caenorhabditis elegans* development. *Annu Rev Genet*. 2024:58:113–134. https://doi.org/10.1146/annurev-genet-111523-102051.

Jorgensen WL, Maxwell DS, TiradoRives J. Development and testing of the OPLS all-atom force field on conformational energetics and properties of organic liquids. *J Am Chem Soc*. 1996:118(45):11225–11236. https://doi.org/10.1021/ja9621760.

Jumper J, Evans R, Pritzel A, Green T, Figurnov M, Ronneberger O, Tunyasuvunakool K, Bates R, Zidek A, Potapenko A, *et al.* Highly accurate protein structure prediction with AlphaFold. *Nature*. 2021:596(7873):583–589. https://doi.org/10.1038/s41586-021-03819-2.

Kanneganti TD. Intracellular innate immune receptors: life inside the cell. *Immunol Rev*. 2020:297(1):5–12. https://doi.org/10.1111/imr.12912.

Karki R, Lee S, Mall R, Pandian N, Wang YQ, Sharma BR, Malireddi RS, Yang D, Trifkovic S, Steele JA, *et al.* ZBP_1-dependent inflammatory cell death, PANoptosis, and cytokine storm disrupt IFN therapeutic efficacy during coronavirus infection. *Sci Immunol*. 2022:7:eabo6294. https://doi.org/10.1126/sciimmunol.abo6294.

Karki R, Sharma BR, Tuladhar S, Williams EP, Zalduondo L, Samir P, Zheng M, Sundaram B, Banoth B, Malireddi RKS, *et al.* Synergism of TNF-α and IFN-γ triggers inflammatory cell death, tissue damage,

and mortality in SARS-CoV-2 infection and cytokine shock syndromes. *Cell*. 2021:184(1):149–168.e17. https://doi.org/10.1016/j.cell.2020.11.025.

Karki R, Sundaram B, Sharma BR, Lee S, Malireddi RKS, Nguyen LN, Christgen S, Zheng M, Wang YQ, Samir P, *et al.* ADAR1 restricts ZBP1-mediated immune response and PANoptosis to promote tumorigenesis. *Cell Rep*. 2021:37(3):109858. https://doi.org/10.1016/j.celrep.2021.109858.

Katoh K, Rozewicki J, Yamada KD. MAFFT online service: multiple sequence alignment, interactive sequence choice and visualization. *Brief Bioinform*. 2019:20(4):1160–1166. https://doi.org/10.1093/bib/bbx108.

Kersse K, Verspurten J, Vanden Berghe T, Vandenabeele P. The death-fold superfamily of homotypic interaction motifs. *Trends Biochem Sci*. 2011:36(10):541–552. https://doi.org/10.1016/j.tibs.2011.06.006.

Kesavardhana S, Malireddi RKS, Kanneganti TD. Caspases in cell death, inflammation, and pyroptosis. *Annu Rev Immunol*. 2020:38(1):567–595. https://doi.org/10.1146/annurev-immunol-073119-095439.

Kischkel FC, Lawrence DA, Tinel A, LeBlanc H, Virmani A, Schow P, Gazdar A, Blenis J, Arnott D, Ashkenazi A. Death receptor recruitment of endogenous caspase-10 and apoptosis initiation in the absence of caspase-8. *J Biol Chem*. 2001:276(49):46639–46646. https://doi.org/10.1074/jbc.M105102200.

Koonin EV, Aravind L. Origin and evolution of eukaryotic apoptosis: the bacterial connection. *Cell Death Differ*. 2002:9(4):394–404. https://doi.org/10.1038/sj.cdd.4400991.

Krissinel E, Henrick K. Inference of macromolecular assemblies from crystalline state. *J Mol Biol*. 2007:372(3):774–797. https://doi.org/10.1016/j.jmb.2007.05.022.

Kuriakose T, Man SM, Malireddi RK, Karki R, Kesavardhana S, Place DE, Neale G, Vogel P, Kanneganti TD. ZBP1/DAI is an innate sensor of influenza virus triggering the NLRP3 inflammasome and programmed cell death pathways. *Sci Immunol*. 2016:1(2):aag2045. https://doi.org/10.1126/sciimmunol.aag2045.

Lee S, Karki R, Wang YQ, Nguyen LN, Kalathur RC, Kanneganti TD. AIM2 forms a complex with pyrin and ZBP1 to drive PANoptosis and host defence. *Nature*. 2021:597(7876):415-+. https://doi.org/10.1038/s41586-021-03875-8.

Li Y, Fu TM, Lu A, Witt K, Ruan J, Shen C, Wu H. Cryo-EM structures of ASC and NLRC4 CARD filaments reveal a unified mechanism of nucleation and activation of caspase-1. *Proc Natl Acad Sci U S A*. 2018:115(43):10845–10852. https://doi.org/10.1073/pnas.1810524115.

Lu C, Wu C, Ghoreishi D, Chen W, Wang L, Damm W, Ross GA, Dahlgren MK, Russell E, Von Bargen CD, *et al.* OPLS4: improving force field accuracy on challenging regimes of chemical space. *J Chem Theory Comput*. 2021:17(7):4291–4300. https://doi.org/10.1021/acs.jctc.1c00302.

Lukens JR, Gurung P, Vogel P, Johnson GR, Carter RA, McGoldrick DJ, Bandi SR, Calabrese CR, Vande Walle L, Lamkanfi M, *et al.* Dietary modulation of the microbiome affects autoinflammatory disease. *Nature*. 2014:516(7530):246–249. https://doi.org/10.1038/nature13788.

Madeira F, Madhusoodanan N, Lee JH, Eusebi A, Niewielska A, Tivey ARN, Lopez R, Butcher S. The EMBL-EBI job dispatcher sequence analysis tools framework in 2024. *Nucleic Acids Res*. 2024:52(W1):W521–W525. https://doi.org/10.1093/nar/gkae241.

Malireddi RKS, Kesavardhana S, Karki R, Kancharana B, Burton AR, Kanneganti TD. RIPK1 distinctly regulates *Yersinia*-induced inflammatory cell death, PANoptosis. *Immunohorizons*. 2020:4(12):789–796. https://doi.org/10.4049/immunohorizons.2000097.

Man SM, Kanneganti TD. Converging roles of caspases in inflammasome activation, cell death and innate immunity. *Nat Rev Immunol*. 2016:16(1):7–21. https://doi.org/10.1038/nri.2015.7.

Man SM, Tourlomousis P, Hopkins L, Monie TP, Fitzgerald KA, Bryant CE. Salmonella infection induces recruitment of caspase-8 to the inflammasome to modulate IL-1beta production. *J Immunol*. 2013:191(10):5239–5246. https://doi.org/10.4049/jimmunol.1301581.

Martinon F, Burns K, Tschopp J. The inflammasome: a molecular platform triggering activation of inflammatory caspases and processing of proIL-beta. *Mol Cell*. 2002:10(2):417–426. https://doi.org/10.1016/S1097-2765(02)00599-3.

Martinon F, Hofmann K, Tschopp J. The pyrin domain: a possible member of the death domain-fold family implicated in apoptosis and inflammation. *Curr Biol*. 2001:11(4):R118–R120. https://doi.org/10.1016/S0960-9822(01)00056-2.

Minh BQ, Schmidt HA, Chernomor O, Schrempf D, Woodhams MD, von Haeseler A, Lanfear R. IQ-TREE 2: new models and efficient methods for phylogenetic inference in the genomic era. *Mol Biol Evol*. 2020:37(5):1530–1534. https://doi.org/10.1093/molbev/msaa015.

Mirdita M, Schütze K, Moriwaki Y, Heo L, Ovchinnikov S, Steinegger M. ColabFold: making protein folding accessible to all. *Nat Methods*. 2022:19(6):679–682. https://doi.org/10.1038/s41592-022-01488-1.

Moore RM, Harrison AO, McAllister SM, Polson SW, Wommack KE. Iroki: automatic customization and visualization of phylogenetic trees. *PeerJ*. 2020:8:e8584. https://doi.org/10.7717/peerj.8584.

Mukherjee S, Zhang Y. MM-align: a quick algorithm for aligning multiple-chain protein complex structures using iterative dynamic programming. *Nucleic Acids Res*. 2009:37(11):e83. https://doi.org/10.1093/nar/gkp318.

Murrell B, Moola S, Mabona A, Weighill T, Sheward D, Kosakovsky Pond SL, Scheffler K. FUBAR: a fast, unconstrained Bayesian approximation for inferring selection. *Mol Biol Evol*. 2013:30(5):1196–1205. https://doi.org/10.1093/molbev/mst030.

Muzio M, Chinnaiyan AM, Kischkel FC, ORourke K, Shevchenko A, Ni J, Scaffidi C, Bretz JD, Zhang M, Gentz R, *et al.* FLICE, a novel FADD-homologous ICE/CED-3-like protease, is recruited to the CD95 (Fas/APO-1) death-inducing signaling complex. *Cell*. 1996:85(6):817–827. https://doi.org/10.1016/S0092-8674(00)81266-0.

Neuwald AF. Rapid detection, classification and accurate alignment of up to a million or more related protein sequences. *Bioinformatics*. 2009:25(15):1869–1875. https://doi.org/10.1093/bioinformatics/btp342.

Neuwald AF. A Bayesian sampler for optimization of protein domain hierarchies. *J Comput Biol*. 2014a:21(3):269–286. https://doi.org/10.1089/cmb.2013.0099.

Neuwald AF. Evaluating, comparing, and interpreting protein domain hierarchies. *J Comput Biol*. 2014b:21(4):287–302. https://doi.org/10.1089/cmb.2013.0098.

Neuwald AF, Altschul SF. Inference of functionally-relevant N-acetyltransferase residues based on statistical correlations. *PLoS Comput Biol*. 2016:12(12):e1005294. https://doi.org/10.1371/journal.pcbi.1005294.

Neuwald AF, Altschul SF. Statistical investigations of protein residue direct couplings. *PLoS Comput Biol*. 2018:14(12):e1006237. https://doi.org/10.1371/journal.pcbi.1006237.

Neuwald AF, Aravind L, Altschul SF. Inferring joint sequence-structural determinants of protein functional specificity. *Elife*. 2018:7:e29880. https://doi.org/10.7554/eLife.29880.

Neuwald AF, Lanczycki CJ, Hodges TK, Marchler-Bauer A. Obtaining extremely large and accurate protein multiple sequence alignments from curated hierarchical alignments. *Database (Oxford)*. 2020:2020:baaa042. https://doi.org/10.1093/database/baaa042.

Neuwald AF, Yang H, Tracy Nixon B. SPARC: structural properties associated with residue constraints. *Comput Struct Biotechnol J*. 2022:20:1702–1715. https://doi.org/10.1016/j.csbj.2022.04.005.

Newton K, Wickliffe KE, Maltzman A, Dugger DL, Reja R, Zhang Y, Roose-Girma M, Modrusan Z, Sagolla MS, Webster JD, *et al.* Activity of caspase-8 determines plasticity between cell death pathways. *Nature*. 2019:575(7784):679–682. https://doi.org/10.1038/s41586-019-1752-8.

Onufriev A, Bashford D, Case DA. Exploring protein native states and large-scale conformational changes with a modified generalized

born model. *Proteins-Struct Funct Bioinf*. 2004:55(2):383–394. https://doi.org/10.1002/prot.20033.
Park HH, Lo YC, Lin SC, Wang L, Yang JK, Wu H. The death domain superfamily in intracellular signaling of apoptosis and inflammation. *Annu Rev Immunol*. 2007:25(1):561–586. https://doi.org/10.1146/annurev.immunol.25.022106.141656.
Paysan-Lafosse T, Blum M, Chuguransky S, Grego T, Pinto BL, Salazar GA, Bileschi ML, Bork P, Bridge A, Colwell L, *et al.* InterPro in 2022. *Nucleic Acids Res*. 2023:51(D1):D418–D427. https://doi.org/10.1093/nar/gkac993.
Pierini R, Juruj C, Perret M, Jones CL, Mangeot P, Weiss DS, Henry T. AIM2/ASC triggers caspase-8-dependent apoptosis in Francisella-infected caspase-1-deficient macrophages. *Cell Death Differ*. 2012:19(10):1709–1721. https://doi.org/10.1038/cdd.2012.51.
Place DE, Lee S, Kanneganti TD. PANoptosis in microbial infection. *Curr Opin Microbiol*. 2021:59:42–49. https://doi.org/10.1016/j.mib.2020.07.012.
Ponder JW, Case DA. Force fields for protein simulations. In: Richards F, Eisenberg D, Kuriyan J, editors. *Advances in Protein Chemistry*. New York: Academic Press; 2003. p. 27–85.
Protein Data Bank in Europe. 2024. Protein interfaces, surfaces and assemblies service PISA at the European Bioinformatics Institute. Available from: http://www.ebi.ac.uk/pdbe/prot_int/pistart.html [Internet].
Reed JC, Doctor KS, Godzik A. The domains of apoptosis: a genomics perspective. *Sci STKE*. 2004:2004(239):re9. https://doi.org/10.1126/stke.2392004re9.
Richardson DC. Reduce [Internet]; 2024. Available from: http://kinemage.biochem.duke.edu/software/reduce/
Robert X, Gouet P. Deciphering key features in protein structures with the new ENDscript server. *Nucleic Acids Res*. 2014:42(W1):W320–W324. https://doi.org/10.1093/nar/gku316.
Sagulenko V, Thygesen SJ, Sester DP, Idris A, Cridland JA, Vajjhala PR, Roberts TL, Schroder K, Vince JE, Hill JM, *et al.* AIM2 and NLRP3 inflammasomes activate both apoptotic and pyroptotic death pathways via ASC. *Cell Death Differ*. 2013:20(9):1149–1160. https://doi.org/10.1038/cdd.2013.37.
Sakamaki K, Imai K, Tomii K, Miller DJ. Evolutionary analyses of caspase-8 and its paralogs: deep origins of the apoptotic signaling pathways. *Bioessays*. 2015:37(7):767–776. https://doi.org/10.1002/bies.201500010.
Sakamaki K, Satou Y. Caspases: evolutionary aspects of their functions in vertebrates. *J Fish Biol*. 2009:74(4):727–753. https://doi.org/10.1111/j.1095-8649.2009.02184.x.
Sakamaki K, Shimizu K, Iwata H, Imai K, Satou Y, Funayama N, Nozaki M, Yajima M, Nishimura O, Higuchi M, *et al.* The apoptotic initiator caspase-8: its functional ubiquity and genetic diversity during animal evolution. *Mol Biol Evol*. 2014:31(12):3282–3301. https://doi.org/10.1093/molbev/msu260.
Sakata S, Yan YL, Satou Y, Momoi A, Ngo-Hazelett P, Nozaki M, Furutani-Seiki M, Postlethwait JH, Yonehara S, Sakamaki K. Conserved function of caspase-8 in apoptosis during bony fish evolution. *Gene*. 2007:396(1):134–148. https://doi.org/10.1016/j.gene.2007.03.010.
Šali A, Blundell TL. Comparative protein modelling by satisfaction of spatial restraints. *J Mol Biol*. 1993:234(3):779–815. https://doi.org/10.1006/jmbi.1993.1626.
Sayers EW, Beck J, Bolton EE, Brister JR, Chan J, Comeau DC, Connor R, DiCuccio M, Farrell CM, Feldgarden M, *et al.* Database resources of the national center for biotechnology information. *Nucleic Acids Res*. 2024:52(D1):D33–D43. https://doi.org/10.1093/nar/gkad1044.
Sborgi L, Ravotti F, Dandey VP, Dick MS, Mazur A, Reckel S, Chami M, Scherer S, Huber M, Bockmann A, *et al.* Structure and assembly of the mouse ASC inflammasome by combined NMR spectroscopy and cryo-electron microscopy. *Proc Natl Acad Sci U S A*. 2015:112(43):13237–13242. https://doi.org/10.1073/pnas.1507579112.
Schrödinger. *PyMOL Molecular Graphics System, Version 3.0*. New York (NY): Schrödinger, LLC; 2024a.
Schrödinger. *Schrödinger release 2024-3: desmond molecular dynamics system*. New York (NY): D. E. Shaw Research; 2024b.
Schrödinger. *Schrödinger release 2024-3: protein preparation wizard; Epik*. New York (NY): Schrödinger, LLC; 2024c.
Seemayer S, Gruber M, Soding J. CCMpred–fast and precise prediction of protein residue-residue contacts from correlated mutations. *Bioinformatics*. 2014:30(21):3128–3130. https://doi.org/10.1093/bioinformatics/btu500.
Sharma BR, Choudhury SM, Abdelaal HM, Wang Y, Kanneganti TD. Innate immune sensor NLRP3 drives PANoptosome formation and PANoptosis. *J Immunol*. 2025:vkaf042. https://doi.org/10.1093/jimmun/vkaf042.
Smith N, Witham S, Sarkar S, Zhang J, Li L, Li C, Alexov E. DelPhi web server v2: incorporating atomic-style geometrical figures into the computational protocol. *Bioinformatics*. 2012:28(12):1655–1657. https://doi.org/10.1093/bioinformatics/bts200.
Spead O, Verreet T, Donelson CJ, Poulain FE. Characterization of the caspase family in zebrafish. *PLoS One*. 2018:13(5):e0197966. https://doi.org/10.1371/journal.pone.0197966.
Sundaram B, Pandian N, Kim HJ, Abdelaal HM, Mall R, Indari O, Sarkar R, Tweedell RE, Alonzo EQ, Klein J, *et al.* NLRC5 senses NAD+ depletion, forming a PANoptosome and driving PANoptosis and inflammation. *Cell*. 2024:187(15):4061–4077.e17. https://doi.org/10.1016/j.cell.2024.05.034.
Sundaram B, Pandian N, Mall R, Wang Y, Sarkar R, Kim HJ, Malireddi RKS, Karki R, Janke LJ, Vogel P, *et al.* NLRP12-PANoptosome activates PANoptosis and pathology in response to heme and PAMPs. *Cell*. 2023:186(13):2783–2801 e2720. https://doi.org/10.1016/j.cell.2023.05.005.
Tondnevis F, Dudenhausen EE, Miller AM, McKenna R, Altschul SF, Bloom LB, Neuwald AF. Deep analysis of residue constraints (DARC): identifying determinants of protein functional specificity. *Sci Rep*. 2020:10(1):1691. https://doi.org/10.1038/s41598-019-55118-6.
Tuckerman M, Berne BJ, Martyna GJ. Reversible multiple time scale molecular-dynamics. *J Chem Phys*. 1992:97(3):1990–2001. https://doi.org/10.1063/1.463137.
Tummers B, Mari L, Guy CS, Heckmann BL, Rodriguez DA, Ruhl S, Moretti J, Crawford JC, Fitzgerald P, Kanneganti TD, *et al.* Caspase-8-dependent inflammatory responses are controlled by its adaptor, FADD, and necroptosis. *Immunity*. 2020:52(6):994–1006.e8. https://doi.org/10.1016/j.immuni.2020.04.010.
Vajjhala PR, Lu A, Brown DL, Pang SW, Sagulenko V, Sester DP, Cridland SO, Hill JM, Schroder K, Stow JL, *et al.* The inflammasome adaptor ASC induces procaspase-8 death effector domain filaments. *J Biol Chem*. 2015:290(49):29217–29230. https://doi.org/10.1074/jbc.M115.687731.
van Zundert GCP, Rodrigues J, Trellet M, Schmitz C, Kastritis PL, Karaca E, Melquiond ASJ, van Dijk M, de Vries SJ, Bonvin A. The HADDOCK2.2 web server: user-friendly integrative modeling of biomolecular complexes. *J Mol Biol*. 2016:428(4):720–725. https://doi.org/10.1016/j.jmb.2015.09.014.
Varadi M, Bertoni D, Magana P, Paramval U, Pidruchna I, Radhakrishnan M, Tsenkov M, Nair S, Mirdita M, Yeo J, *et al.* AlphaFold protein structure database in 2024: providing structure coverage for over 214 million protein sequences. *Nucleic Acids Res*. 2024:52(D1):D368–D375. https://doi.org/10.1093/nar/gkad1011.
Wang JY, Chitsaz F, Derbyshire MK, Gonzales NR, Gwadz M, Lu SN, Marchler GH, Song JS, Thanki N, Yamashita RA, *et al.* The conserved domain database in 2023. *Nucleic Acids Res*. 2023:51(D1):D384–D388. https://doi.org/10.1093/nar/gkac1096.
Wang Y, Kanneganti TD. From pyroptosis, apoptosis and necroptosis to PANoptosis: a mechanistic compendium of programmed cell death pathways. *Comput Struct Biotechnol J*. 2021:19:4641–4657. https://doi.org/10.1016/j.csbj.2021.07.038.
Wang Y, Pandian N, Han JH, Sundaram B, Lee S, Karki R, Guy CS, Kanneganti TD. Single cell analysis of PANoptosome cell death complexes through an expansion microscopy method. *Cell Mol Life Sci*. 2022:79(10):531. https://doi.org/10.1007/s00018-022-04564-z.

Weng GQ, Wang EC, Wang Z, Liu H, Zhu F, Li D, Hou TJ. HawkDock: a web server to predict and analyze the protein-protein complex based on computational docking and MM/GBSA. *Nucleic Acids Res*. 2019:47(W1):W322–W330. https://doi.org/10.1093/nar/gkz397.

Xiong Q, Yang KY, Zeng X, Wang M, Ng PK-S, Zhou J-W, Ng JK-W, Law CT-Y, Du Q, Xu K, *et al*. 2023. Gene novelties in Amphioxus illuminate the early evolution of deuterostomes. bioRxiv 492404. https://doi.org/10.1101/2022.05.18.492404, 6 October 2023, preprint: not peer reviewed.

Zheng MK R, Vogel P, Kanneganti TD. Caspase-6 is a key regulator of innate immunity, inflammasome activation and host defense. *Cell*. 2020:181(3):674–687.e13. https://doi.org/10.1016/j.cell.2020.03.040.